# 5

# Wireless Body Area Communications

**Chapter Editors: R. D'Errico and K. Yekeh Yazdandoost,**
**Section Editors: R. Rosini, K. Sayrafian, T. Kumpuniemi,**
**S. Cotton and M. Mackowiak**

## 5.1 Introduction

With the increasing interest in implantable and wearable technologies for healthcare, diagnosis and health supports by means of wireless connectivity, we are entering in a new era of communications. The wireless body area network (WBAN) is a wireless network technology with purpose to transmit data by implantable or wearable devices to the point of needs [Rei12]. The fundamental idea is to transfer the vital signs of a patient, sportsman, fireman, and so on, collected by sensors to the respectful cotrol unit for further action [BDH+11, Dru07, Rei11, PDRR+12a, PW10b]. Wireless medical information and communication technology will revolutionise health diagnosis and monitoring, with its huge number of possible applications, in home, hospital, and any places where healthcares are provided.

Besides medical applications [PDRR+12b], WBANs are providing new functionalities in peoples' everyday life such as sport, leisure, gaming, and social networks. Watches, glasses, earphones, and bracelets are the most popular, but there are dozens of other wearable and implantable devices which a person could carry in the future. In some sense, grouping those devices into a small network coordinated by the central personal device, which today is the "phone", may change it to become the "router" of WBAN.

The radio channel is central to the paradigm of WBANs [RMM+], and its modelling demands for a different approach when compared to the other know radio propagations [VZ12, YYSP10]. In particular, ANTs play an important role in the context of WBANs (Section 5.2), being affected by the close proximity to the body.

Given the wide range of applications, WBAN communications could be categorised into:

*Cooperative Radio Communications for Green Smart Environments, 151–194.*

- In-Body (Section 5.3), where at least one node of the network is located inside the human body and it should communicate with one or more devices either in, on, or off the body;
- On-Body (Section 5.4), where all the nodes involved in the communication are placed on the human body, either directly stitched on the skin, integrated into textile and worn by the subject;
- Off-Body (Section 5.5), where at least one of the devices is placed outside the human body, located everywhere in a general area playing the role of a gateway or an access point (AP). A particular subset is body-to-body (B2B) communications where both transmitter (TX) and receiver (RX) are placed on two different subjects.

Based on the exact knowledge of the radio channel cooperative and energy-optimised PHY–MAC procotocol can be designed and evaluated (Section 5.6). This chapter provides an overview of the last advances in research on WBANs, carried out in the framework of IC1004 action, and proposes a radio CM whose parameters are reported in Section 5.7.

## 5.2 ANT Design and Modelling

Antennas have an important role in the wireless communication and in particular in WBANs, where small ANTs are required that allows integration into WBAN devices. Placing an ANT inside or close proximity to human body will have severe effect on the ANT characteristics. hence, designing an ANT with high radiation performance that is optimised for these application is very challenging [Wei13]. In order to obtain a reliable wireless communication link, the human body has to be characterised as amedium for wave propagation [YY11a, YY11b]. The influence of the body, which can be considered as an irregularly shaped dielectric medium, on the ANT depends on the body's electrical parameters [MOC12b]. Human tissues have their own unique conductivity, dielectric constant, and characteristic impedance, that determine different degrees and types, of radio frequency (RF) electromagnetic interaction [YM12]. There are large number of ANTs (electrical and magnetic [YY09]) for WBAN applications and it is rather difficult to specify an ideal ANT for every application. Since design of WBAN ANTs are implicated with human body tissues, numerical simulation tools can provide substantial insight into the ANT design mechanisms.

### 5.2.1 Implant ANTs

An efficient ANT is a primary requirement for reliable medical implanted communication. The implanted ANT should be well matched inside a highly

dissipative medium [DEY09, YYM12a, YY12]. The bandwidth limitation at lower frequencies such as industrial, scientific and medical (ISM) and MICS bands force the designer to the higher band such as ultra-wide band (UWB) to provide enough bandwidth that's required to transfer data images for application such as wireless endoscopy. The requirements, complexities, and difficulties to design an inbody ANT, make it impossible to use conventional ANT design of free space for body implanted applications.

In Yazdandoost and Miura [YYM12a, YY13b, YY14a, YY14b], ANT performance analysis is based on simulations. A 3D full-wave electromagnetic field simulator based on finite element method (FEM) has been used. Fabricated prototype is presented in Yazdandoost and Miura [YY13b, YY14b]. Figure 5.1 shows an example of the implant UWB ANT prototype [YY13b]. The ANT has dimension of $10 \times 7.5 \times 1.91$ mm and made on Rogers 6010 substrate with dielectric constant of 10.2 mm and thickness of 0.508 mm. The ANT is covered by Duroid sheet on the top and bottom in order to prevent the effect of the human body tissues on ANT performance. Duroid sheet was sited with help of adhesive material with relative permittivity of 3.7 mm and thickness of 0.02 mm [YY13a, YY13b]. The 10 dB return loss is achieved for the entire UWB band.

### 5.2.2 On-Body ANTs

The presence of body leads to changes in the ANT radiation pattern, shift of the resonance frequency (due to changes in input impedance) and reduction of ANT efficiency. Hence, statistical analysis of ANT performance close proximity to the human body is required, as ANT performance depends strongly on the frequency of usage, on distance to the body, location, and type of body tissues [MOC12b]. Full-wave simulation with realistic models of the human body are a powerful tool to study WBAN scenarios. In Machkowiak et al. [MOC12a], the ANT radiation characteristics is studied with respect to

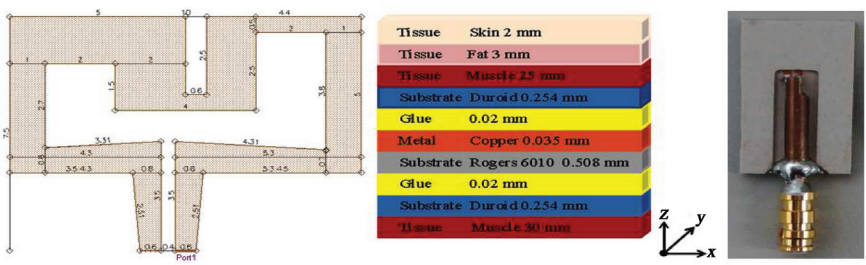


**Figure 5.1** Implant ANT layout [YY13a] ©2013 and prototype [YY13b].

the ANT separation from body. Comparisons are done with simulation and measurements and a pattern average differences of 0.9 dB is found.

Different ANT designs are presented in [GHP+12, MOC12b, YM12, YM13] at 2.4 GHz with linear and circular polarisations. A wearable, electrically small loop ANT is presented in Giddens et al. [GHP+12]. The ANT is printed on Duroid substrate with relative permittivity of 10.2 and thickness of 1 mm. Substrate is separated from ground plane with foam which has a thickness of 4 mm. A large textile ground plane with dimensions of $160 \times 230$ mm$^2$ was attached to the ANT, in order to cancel out the effects of the human body. ANT geometry is shown in Figure 5.2. The measured results show that ANT is resonant at 2.42 GHz and has –10 dB bandwidth of 68 MHz.

The creeping wave is a surface wave along a curvature that reaches the receiving site by traveling along the surface of body. Creeping wave ANTs are receiving much attention in the recent days for on-body application in particular, when two devices are placed on the body surface, and the wireless communication is affected by the body itself [YM12]. To enhance creeping waves, it is necessary to have a vertically polarised ANT. A 2.4-GHz creeping wave loop ANT, on FR4-epoxy substrate with deictic constant of

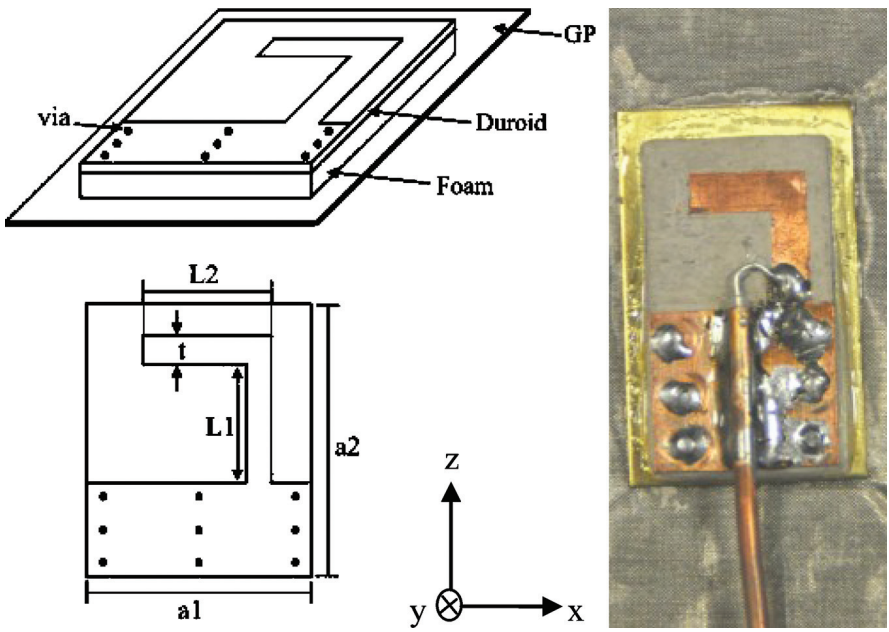


**Figure 5.2** Wearable, electrically small, and magnetically coupled loop ANT: geometry and prototype [GHP+12].

4.4 and thickness of 1 mm, is shown in Figure 5.3. ANT has dimension of $34 \times 10\,\mathrm{mm}^2$ and no ground plane. In Figure 5.3, the simulated electric field is shown and proven to be at a 90-deg. angle with respect to the ANT surface [YY11a, YM12].

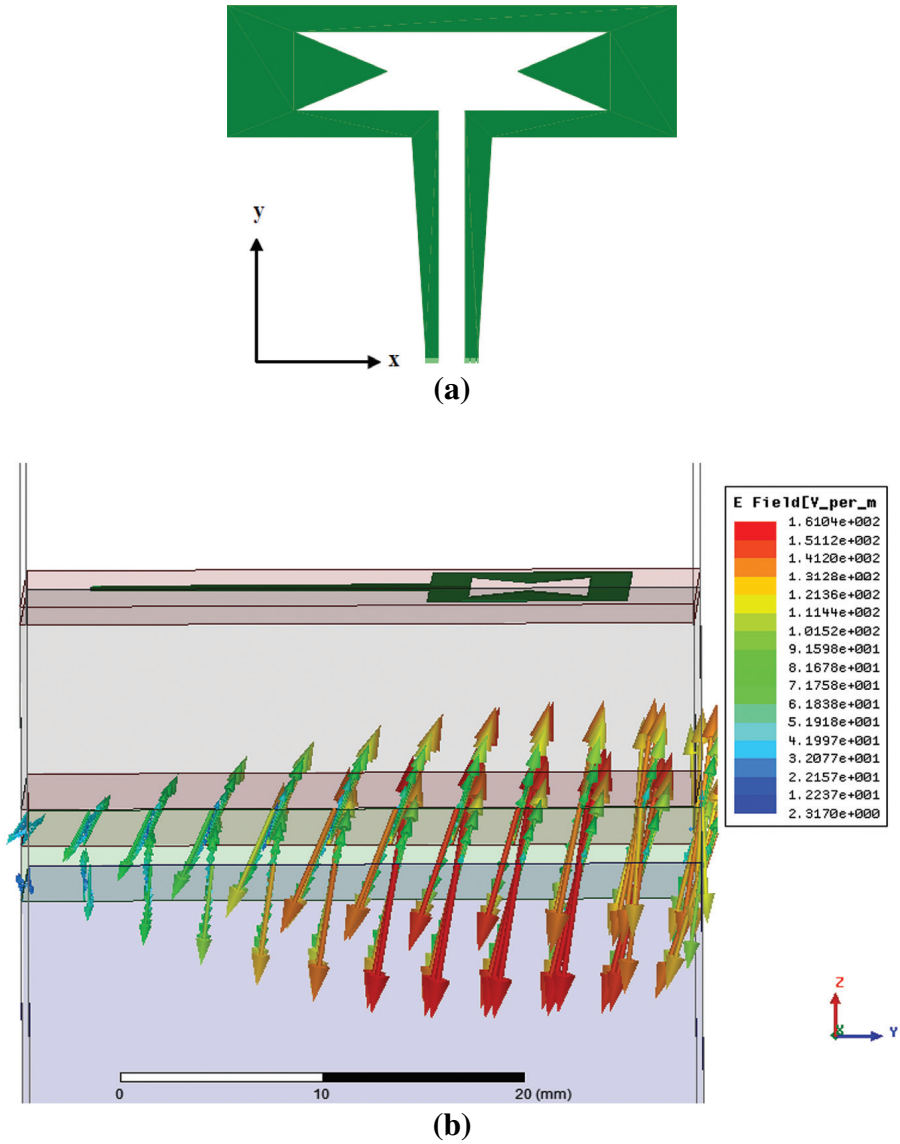


**Figure 5.3** Creeping wave ANT and its vector electric field [GHP+12, YY11a] ©2011.

As narrowband ANTs, the performance of UWB are strongly dependent on the environment of operation. Hence, a challenge for the design of UWB WBAN ANTs remains their potential sensitivity to the proximity of human body, which is due to the strong coupling effect between body tissues and the reactive field of ANT [NC11, WR12, WR13, YY06]. A MSA-BP with operating frequency from 3.38 to 6.07 is presented in Wei and Roblin [WR12]. A back plane is introduced for the reduction of the backward radiation, producing a screening effect between the radiation and the body. ANT has overall sise of $68.1 \times 41.98 \times 4.445\,\mathrm{mm}^3$ and is fed by a tapered CPW line, which provides wideband matching. The ANT geometry and its return loss are presented in Figure 5.4. Desensitisation of the MSA-BP was studied by measuring the refection coefficient on human body and measuring the radio links on a human body phantom. Measurement results confirmed that

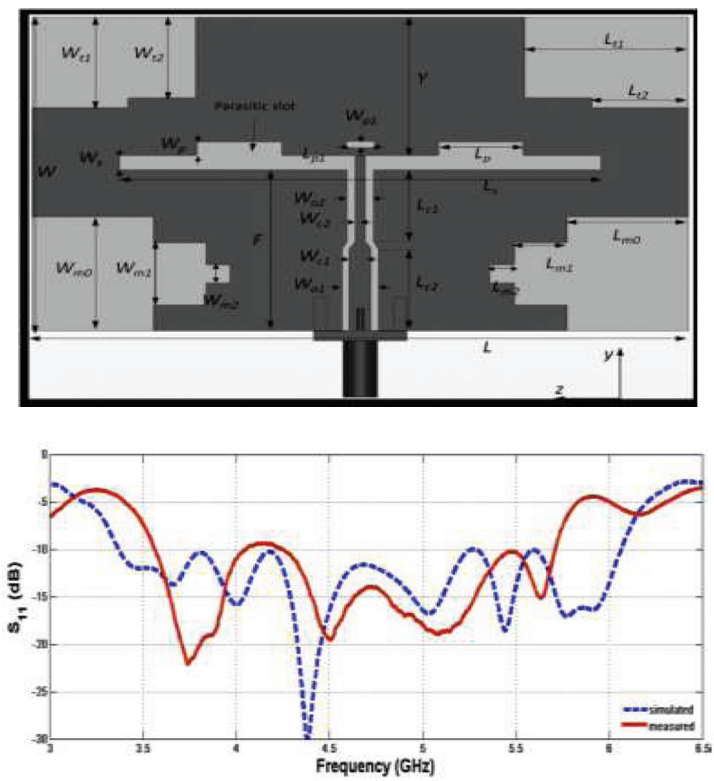


**Figure 5.4** Geometry of the MSA-BP ANT and its simulated and measured return loss [WR12].

the MSA-BP is insensitive to the body proximity. A CFSA is presented in Figure 5.5 [Wei13]. The ANT sise is $21.06 \times 25.2 \times 0.8\,\mathrm{mm}^3$ with bandwidth of 3–12.5 GHz. Further investigation on UWB ANTs for WBAN applications have been addressing the modelling of ANT–body interaction. A simple model based on spherical harmonics coefficient to represent an ANT pattern, allowing to predict a disrupted ANT behaviour by a human phantom with respect to the ANT-phantom distance is presented in [MB13].

WBAN devices are battery operated, energy recharging could be one of the option to avoid of battery replacement. In Barroca et al. [BSG+13], an ANT with necessary circuits for ambient energy harvesting is presented. The ANT is designed for Global Systems Mobile, GSM900, and GSM1800, as they are most promising bands for RF energy harvesting. The ANT has efficiency of 77.6–84% and gain of 1.8–2.06 dBi.

The importance of polarisation in WBAN communication is due to fact that the user will change his positions in the different angles during his activities. A circular polarised ANT can be used when the opposite ANT (TX) polarisation is not defined. Since polarisation of a linearly polarised radio wave may be rotated as the poses of subject is changed. Circular polarisation will keep the signal constant regardless of these difference [YM13, YY13b]. Design and performance of linearly and circularly polarised ANTs are discussed in Yazdandoost and Miura [YM13, YY13b].

The WBAN CM includes ANT effects, hence, ANT will be part of channel [YY10]. De-embedding method for body area network (BAN) is aiming to remove this effect [Aoy13, ATK14b]. In this method, an ANT in proximity to human body is characterised by a small sphere, which surrounds human body (represented by dielectric material) and an ANT. Certain number of multi-poles which represents ANT radiation are set inside the sphere and expansion

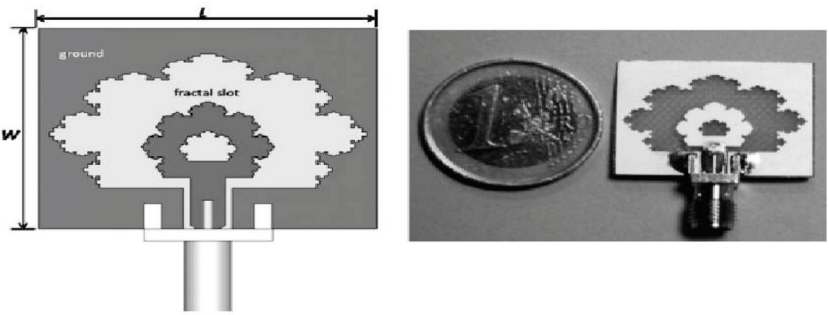


**Figure 5.5** Configuration and prototype of CFSA [Wei13].

coefficients are determined to match boundary conditions on the surface of the sphere. To characterise an ANT in this method, radiated electric and magnetic fields are needed in certain number of matching points on the surface of the sphere. In Aoyagi et al. [AKT13], de-embedding is presented for WBAN ANT at 400 MHz, and in Aoyagi et al. [AKT14a] for an ANT at 430 MHz, and finally de-embedding at 2450 MHz is presented in Aoyagi et al. [ATK14b].

## 5.3 In-Body Radio Channel

Implantable devices offer a myriad of new and exciting medical applications such as implantable pills for precise targeted drug delivery, glucose monitors, bladder pressure monitors, smart capsule endoscopes, and micro robots operating inside the body for biopsy and therapeutic procedures [AMR07]. However, since the early stage of the WBAN standardisation process, it was recognised that modelling the radio channel for implant communication would be a great challenge. Because of a number of ethical and technical issues, measurement campaigns inside living human bodies are not possible. Hence, in order to characterise the propagation of radio signals through human tissues, researchers first carry out numerical simulations of electromagnetic waves propagation using a digital anatomical model or liquid phantoms. Then, the obtained data can be processed statistically to produce simulation or measurement-based models. This section outlines research studies related to implant radio channels that were presented during the COST IC1004 sessions.

Propagation models play a critical role in designing reliable and efficient wireless communication link. Authors Yazdandoost and Miura [YY11c] provide a theoretical investigation on the communication radio channel for body implantable devices based on specific absorption rate (SAR). Their study elaborates on the importance of factors such as near/far-field attenuations as well as ANT placement and orientation inside the body. By determining the average SAR over the entire mass of tissue between the TX and RX, they compute the total attenuation due to the human body. SAR is a standard measure of how much power is absorbed in the body tissue. The absorbed power is lost due to heat dissipation. The amount of this power depends on the strength of the E-field and H-field. In general, the propagation loss between the transmitting and the receiving ANTs (assuming that one is implanted) is dependent on thermal attenuation due to conductivity, reflection losses at tissue boundaries, and near-field and far-field losses. This loss is naturally a function of frequency and distance. Analysis in Yazdandoost and Miura [YY11c] indicates that these factors can not only affect the amount of radiation inside the human body, but also determine the optimum distance at which a reliable

performance in the implant communication link can be achieved. UWB radio technology has inherently desirable characteristics (i.e., high data rate and low power) that make it highly suitable for the radio interface of implant sensors. However, there are currently few models that characterise the UWB radio propagation inside the human body. To address this problem, authors Chvez-Santiago and Balasingham [CS14a] present a statistical model for UWB propagation channels inside the human chest in the 16 GHz frequency range. The proposed statistical model is developed from numerical simulations using a heterogeneous anatomical model that includes the frequency-dependent dielectric properties of various human tissues. Their results show that the channel characteristics vary considerably at different depths inside the human body. Therefore, a depth-dependent statistical channel model (CM) for the frequency range 16 GHz has been proposed. This statistical model facilitates the realisation of a distorted pulse after propagating through human tissues. This is very beneficial for the design and evaluation of UWB transceivers, as well as generation of signal templates for correlator RXs and synchronisation schemes. As mentioned before, this study only considered the human chest. Due to the highly inhomogeneous structure of the human body, a customised model may be derived for other parts of the body. The work by Chvez-Santiago and Balasingham [CS14a] has established some guidelines for the development of such models. One of the most innovative applications of radio communication technology inside the human body is wireless capsule endoscope (WCE). This electronic device helps to examine hard-to-reach parts of the gastrointestinal (GI) tract with significantly less discomfort for the patient than traditional wired endoscopic methods. The use of an UWB radio interface, which can enable high data rate transmission, would significantly enhance the information (i.e., video) quality for a WCE device. However, the high attenuation of radio signals propagating through living tissues infrequencies above 1 GHz make the use of UWB radio links for this application quite challenging. Authors Chvez-Santiago and Balasingham [CS13] have presented several ideas to overcome this challenge. These ideas include: selecting the proper implantable ANT, increasing the transmit power, exploiting spatial diversity, and using a dielectric matching layer. Their simulation-based and experimental (i.e., *in vivo* animal test) studies suggest that the implementation of such a UWB communication link for the implantable device is feasible. Future medical applications may also require communication among two or more implanted devices, for example, to exchange information for better diagnostics or to relay data from sensors deep inside the human body. For such applications, authors in Chavez-Santiago et al. [CS14b] propose the use of UWB radios as a communication interface between in-body sensors.

An implant-to-implant statistical CM at the MICS band (i.e., 401–405 MHz) has been presented in Sayrafian et al. [Say10]; however, less information is available regarding the characteristics of implant-to-implant radio channel in the UWB spectrum. The work presented in [CGF14] provides insight into the behaviour of the implant-to-implant radio channel based on propagation measurements in the 3.1–8.5 GHz frequency range. As it is nearly impossible to conduct in-body measurements with human subjects, a liquid phantom that emulated the dielectric characteristics of the human muscle tissue has been used in these measurements. The initial qualitative analysis indicates the feasibility of UWB communication between two implanted sensors; however, the frequency-dependent attenuation of the channel imposes the need for a careful selection of the operating frequency band. Based on the measurements results, the authors in [CGF14] indicate that the most appropriate frequency band for general in-body to in-body UWB communications is 3.1–4.6 GHz. For specific applications in which the transmission range is very short (i.e., below 60 mm) higher frequencies can also be used. It should be noted that the liquid phantom used for the measurement is a homogeneous propagation medium with a single dielectric constant. This contrasts the human body which is a non-homogeneous structure of multiple biological tissue layers with different dielectric constants. Therefore, the validation of the propagation models derived from phantom measurements has to be done either through numerical simulations using a digital model of the humanbody or through *in vivo* measurements on chirurgical animal models.

## 5.4 On-Body Radio Channel

This section presents the results obainted in terms of channel characterisation and modelling for on-body communications. Several measurement campaings were carried out in different bands. Here for sake of clarity, we divide between UWB and narrowband channels. Final model parameters are reported in Section 5.7.

### 5.4.1 UWB On-Body Channel

#### 5.4.1.1 Channel characterisation

In Llorca et al. [LBC12], two static measurement campaigns were conducted in an anechoic chamber and office environment by using VNAs in the 3–6 GHz and 1–12 GHz frequency bands. The TX was placed on top, right or left side or back of the head. Six arm positions with RX in hand, and cases when the RX lay in 12 spots along the front and back torso, right arm and foot were

measured. The original 50 taps long CIRs were modelled with 24, 12, and 6 taps and the resulting error from the exact channel impulse response (CIR) was observed.

Yazdandoost and Miura [YYM12b] report simulation results for UWB on-body channels with an L-shaped loop ANT within the frequency range of 3.1–5.1 GHz. The RX positions were at the chest, and left and right ear, shoulder and waist. The TX was located either at the abdomen, right waist or left wrist. The path loss (PL) models were extracted both at discrete frequencies and the full frequency range with different TX locations.

Kumpuniemi et al. [KTH+13] present static measurements conducted in an anechoic chamber at a 2–8 GHz range using a four-port vector network analyzer (VNA) and two planar prototype ANT (dipole and double loop). The ANT spots were at the top of the head, left and right ear, right shoulder, upper left chest, left arm, wrist, waist, patella and ankle, right wrist and hip, and right hand first finger tip. From the CIR, PL models were derived CM, static. If the link distances are solved from the CIR, the propagation delay in the ANT must be compensated, or the results especially in short link distances may be affected.

In Kumpuniemi et al. [KHT+13], the data was utilised to produce CIR envelope models and small-scale CM. The statistical characteristics for the CIR amplitude and maximum CIR tap number were obtained.

Kumpuniemi et al. [KHT+14] develop pseudo-dynamic CM, a pseudo-dynamic with the measurement setup as in Kumpuniemi et al. [KTH+13]. The ANT lay at left and right wrist, and left ankle. Five static body postures describing a walking cycle were measured and the data was combined to model a dynamic movement. The attenuations of the first–arriving CIR paths were observed. Then the links were sorted into groups of line-of-sight (LOS), obstructed line-of-sight (OLOS) and non-line-of-sight (NLOS), and the distributions of the CIR taps were solved. Figure 5.6 shows the graphs of the average categorised CIR.

Kumpuniemi et al. [KHYI14] examines channel differences between humans with the equipment used in Kumpuniemi et al. [KTH+13]. Three males and one female were measured. The ANT were at the abdomen, left ankle, right wrist and lumbar region. The PL of the first arriving paths, excess delays, and cross-correlation coefficients between the links were solved.

Kumpuniemi et al. [KHYI15] presents dynamic CM, dynamic for discrete frequencies based on measurements with the setting as in Kumpuniemi et al. [KTH+13]. The ANT were located at the abdomen, left and right ear and wrist, chest, left shoulder and ankle. Both uniform and mixed ANT scenarios

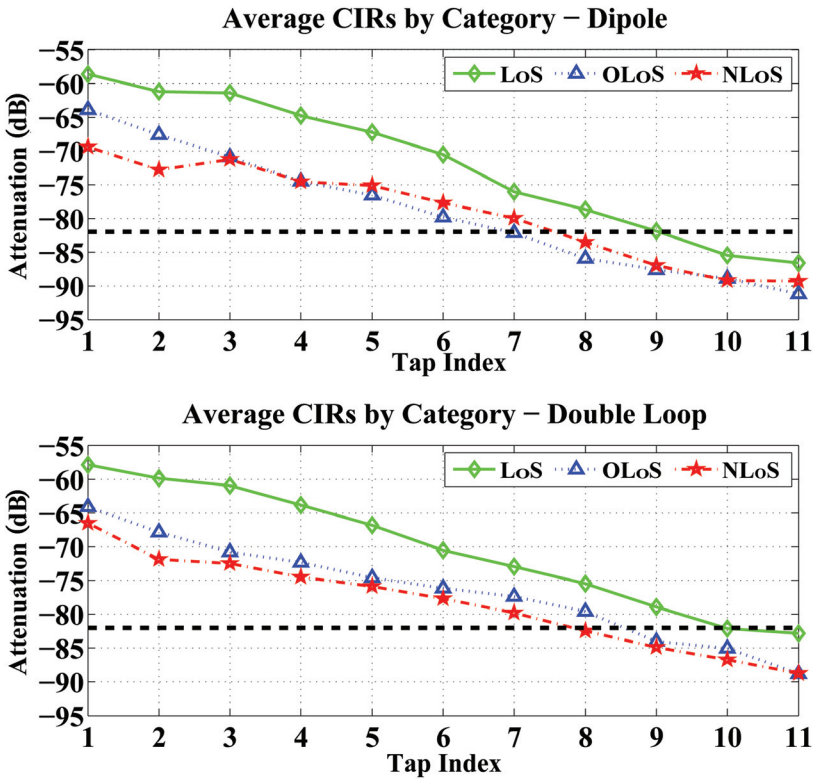


**Figure 5.6** Average categorised CIR.

were examined. First, the links were examined at 10 frequencies. Then, the links were categorised into channel types with high dynamic (HD), medium dynamic (MD) and low dynamic (LD), and their probability distributions were found out.

Wang [Wan14] shows dynamic UWB MIMO measurements with a Medav channel sounder at 3.5–10.5 GHz. At first, two TX and four RX wearable fabric made ANT were attached on wrist, knee, foot, or chest. Then, two TX and two RX ANT lay at the eye, wrist or chest, and two omni-directional ANT acted as an off-body RX of an AP. Four body motions were recorded and the channel gain was considered.

Wang and Bocus [WB14a] extend the work by [Wan14]. Graphs of the channel gain, root-mean-square delay spread, ray number, level crossing rate (LCR), average fading duration, multi-link, and temporal auto-correlation function are visualised.

#### 5.4.1.2 Channel model

In Yazdandoost and Miura [YYM12b], the PL models at a distance d follow the equation:

$$\mathrm{PL}(d) = \mathrm{PL}(d_0) + 10 \cdot n \cdot \log_{10}\left(\frac{d}{d_0}\right) + S, \tag{5.1}$$

where $d_0$ is the reference distance 50 mm, PL($d_0$) is the path loss (PL) in dB at $d_0$, $n$ is the PL exponent, and $S$ is the normally distributed random scattering term with N (0, $\sigma_S^2$). The values lie between PL($d_0$) = 18.90 ... 41.54 dB, $n$ = 1.40 ... 2.85, and $\sigma_S$ = 2.40 ... 9.72 dB depending on the TX location and whether full frequency band or discrete frequencies are considered.

Kumpuniemi et al. [KTH+13] explains PL models based on Equation (5.1) with the parameter values PL($d_0$) = 31.6 (20.4) dB, $n$ = 3.3 (3.1), and $\sigma$ = 12.8 (11.6) dB for the dipole, and PL($d_0$) = 39.8 (25.1) dB, $n$ = 2.7 (2.6), and $\sigma$ = 13.8 (12.2) dB for the loop, depending on whether the first or all arriving paths (in brackets) are considered.

In Kumpuniemi et al. [KHT+13], the statistical CM are solved by fitting the amplitudes of the CIR against several continuous distributions and ranking them with the second order akaike information criterion (AICc). The CM for the dipole base on the Weibull distribution and the lognormal distribution. The double loop CIR amplitude follows the inverse Gaussian distribution. The probability density function (PDF) of the Weibull, lognormal, and inverse Gaussian distributions have the Equations (5.5), (5.4), and (5.3). Their parameter values are listed in Table 5.1.

**Table 5.1** Parameters for the static UWB on-body CM

| Tap | Dipole | Double Loop |
|---|---|---|
| 1 | $a$ = 0.0012, $b$ = 0.8147 | $\alpha$ = 0.0011, $\beta$ = 1.0413 × $10^{-4}$ |
| 2 | $a$ = 5.7829 × $10^{-4}$, $b$ = 0.7795 | $\alpha$ = 6.3532 × $10^{-4}$, $\beta$ = 3.5521 × $10^{-5}$ |
| 3 | $a$ = 4.8969 × $10^{-4}$, $b$ = 0.7345 | $\alpha$ = 6.4157 × $10^{-4}$, $\beta$ = 4.5918 × $10^{-5}$ |
| 4 | $\mu$ = −8.6100, $\sigma$ = 1.4787 | $\alpha$ = 4.8655 × $10^{-4}$, $\beta$ = 5.0342 × $10^{-5}$ |
| 5 | $\mu$ = −8.9040, $\sigma$ = 1.4142 | $\alpha$ = 3.3322 × $10^{-4}$, $\beta$ = 3.1961 × $10^{-5}$ |
| 6 | $\mu$ = −9.2348, $\sigma$ = 1.4082 | $\alpha$ = 2.4969 × $10^{-4}$, $\beta$ = 3.7238 × $10^{-5}$ |
| 7 | $\mu$ = −9.4845, $\sigma$ = 1.2954 | $\alpha$ = 1.9503 × $10^{-4}$, $\beta$ = 4.0707 × $10^{-5}$ |
| 8 | $\mu$ = −9.7374, $\sigma$ = 1.3346 | $\alpha$ = 1.4940 × $10^{-4}$, $\beta$ = 3.7844 × $10^{-5}$ |
| 9 | $\mu$ = −9.9844, $\sigma$ = 1.2842 | $\alpha$ = 1.2693 × $10^{-4}$, $\beta$ = 2.5836 × $10^{-5}$ |
| 10 | $\mu$ = −10.1519, $\sigma$ = 1.3819 | $\alpha$ = 1.2102 × $10^{-4}$, $\beta$ = 2.2066 × $10^{-5}$ |
| 11 | $\mu$ = −10.3447, $\sigma$ = 1.4312 | $\alpha$ = 1.0046 × $10^{-4}$, $\beta$ = 1.7603 × $10^{-5}$ |
| 12 | – | $\alpha$ = 7.7384 × $10^{-5}$, $\beta$ = 1.5076 × $10^{-5}$ |

The mean PL of the first arriving CIR path in Kumpuniemi et al. [KHT+14] range between 54.6 and 85.6 dB. The categorised CM describe the linearly scaled relative CIR tap amplitudes of the LoS, OLoS, and NLoS classes. The inverse Gaussian distribution distribution obtained the best AICc ranking and its parameter values are described in Kumpuniemi et al. [KHT+14].

In Kumpuniemi et al. [KHYI15], the mean PL lay between 32.8 and 80.6 dB and the standard deviation of the PL between 0.6 and 12.9 dB depending on the link and frequency. The dynamic HD, MD, and LD CM are based on the inverse Gaussian distribution, and they describe the linearly scaled relative amplitudes of the received discrete frequency signals. The distribution parameters for the models are gathered in Table 5.2.

## 5.4.2 Narrow Band On-Body Channel

### 5.4.2.1 Channel characterisation

Characterisation of the narrow band on-body channel within the remit of IC1004 TWGB has been performed using a range of methods including analytical modelling, simulation, and various channel measurement campaigns. Analytical modelling of on-body channels has been investigated in Chandra

**Table 5.2** Parameters for the dynamic UWB on-body CM

| | | | Link Type | | |
|---|---|---|---|---|---|
| | | | *HD* | *MD* | *LD* |
| ANT Type | Freq. (MHz) | Param. | $\times\ 10^{-4}$ | $\times\ 10^{-4}$ | $\times 10^{-4}$ |
| | 2450.0 | $\alpha$ | 26.75 | 69.66 | 97.39 |
| | | $\beta$ | 3.55 | 17.69 | 33.25 |
| *Uniform* | 3995.0 | $\alpha$ | 14.45 | 85.16 | 65.96 |
| *Dipole* | | $\beta$ | 9.71 | 3.72 | 7.31 |
| | 7988.2 | $\alpha$ | 16.87 | 25.35 | 42.40 |
| | | $\beta$ | 2.98 | 1.50 | 3.63 |
| | 2450.0 | $\alpha$ | 20.51 | 21.62 | 68.59 |
| | | $\beta$ | 1.92 | 20.39 | 20.55 |
| *Uniform* | 3995.0 | $\alpha$ | 17.17 | 32.63 | 50.55 |
| *Loop* | | $\beta$ | 1.25 | 3.98 | 3.23 |
| | 7988.2 | $\alpha$ | 10.26 | 26.88 | 67.09 |
| | | $\beta$ | 2.22 | 1.30 | 10.23 |
| | 2450.0 | $\alpha$ | 46.48 | 144.46 | none |
| | | $\beta$ | 53.04 | 751.86 | none |
| *Mixed* | 3995.0 | $\alpha$ | 13.38 | 81.33 | none |
| *Dipole/Loop* | | $\beta$ | 14.08 | 44.64 | none |
| | 7988.2 | $\alpha$ | 4.04 | 60.33 | none |
| | | $\beta$ | 3.69 | 47.44 | none |

and Johansson [CJ13]. Here, the authors initially represented the human torso as an elliptical surface and studied the attenuation of the creeping wave. The ear-to-ear propagation channel was also investigated, and using FDTD-based simulations conducted at 2.45 GHz, good agreement was shown to exist between the proposed model and the simulations.

In the future, short-range high-bandwidth links with sensors and APs situated in the local environment will allow rapid data transfer to and from WBAN nodes. Representing the human body as a cylinder, an analytical model for the 60 GHz off-body channel has been presented in Mavridis et al. [MPDD+13]. Segmenting the analysis into 'lit' and 'shadowed' regions the proposed models have been shown to provide good agreement with physical (PHY) measurements, considering both transverse electric and transverse magnetic polarisations for illumination of the body by a 60-GHz wave. The authors of this study have also defined an extremely useful transition operator which enables the conversion of the IEEE 802.11ad indoor CM defined in Maltsev et al. [Mal+10] into an off-body CM.

Conducting body centric channel measurements at millimeter wave frequencies such as 60 GHz presents many challenges not least due to the high cable losses, but also sweep repetition rates if scanning wide bandwidths using VNAs. To overcome some of these limitations, a novel frequency-modulated continuous wave (FMCW) measurement system for 60 GHz channel measurements has been developed in Salous et al. [SNCC13]. Using FMCW channel sounder, on-body and short-range off-body channel measurements have been made at 60 GHz. To illustrate its effectiveness, the output of the new FMCW channel sounder was compared with the results of on-body channel measurements obtained from a VNA. The vastly superior sampling capability of the FMCW channel sounder meant that it was able to sweep 4.4 GHz of bandwidth in 819.2 μs compared to 411 s for the VNA. As a result, the authors noted more dispersion prior to the main peak in the power delay profile (PDP) for the VNA measurements compared to those acquired using the channel sounder for the same ANT configuration and body scenario. The authors of Salous et al. [SNCC13] reason that this was due to the exceptionally long acquisition time of the VNA, meaning that this dispersion could have been due to movement during the sweep time.

With the exception of Aoyagi and Takada [AT11] and Mhedhbi et al. [MAAU14], simulation of on-body channels has primarily been conducted using the finite-difference time-domain (FDTD) method [CJ11, CJ13, KJVM11, YYM12a]. For example in Yazdandoost and Miura [YYM12a], the FDTD method is used to investigate the creeping wave mode of propagation

around a cylinder representing the human body at 2.4 GHz. To ensure that they were simulating the creeping wave component of the on-body channel, the authors Yazdandoost and Miura [YYM12a] placed their ANTs on opposite sides of the body to guarantee NLoS channel conditions. It should be noted that the ANTs used in this study were purposely designed to maximise coupling over the body surface by enhancing the creeping wave component.

Using the FDTD method to simulate wave propagation at 2.45 GHz between a pace maker acting as a central hub and multiple implant locations such as the liver, heart, spleen, and the kidneys, a PL model for a heterogeneous human model was developed in Kurup et al. [KJVM11]. For in-body communications, the authors state that increases in PL depend on two factors, namely the distance between the implants and the tissues and organs through which the propagation takes place with front-to-back propagation particularly susceptible to high PL. Adhering to SAR guidelines, a link budget equation for wireless communications between implanted devices has also proposed.

As an alternative to the FDTD method, the work presented in Aoyagi and Takada [AT11] proposes the use of the generalised multipole technique (GMT) technique [Haf90] to model WBAN propagation. More recently, graph based ray tracing for the purpose of on-body channel modelling has been investigated in Mhedhbi et al. [MAAU14]. The simulations used a motion capture sequence to model body movement and a perturbed model of a patch ANT operating at 2.4 GHz, taking into account the body presence. The output of the simulator was compared with open source channel data provided by NICTA [NIC12] covering a wide range of body positions such as the ankle, back, chest, hip, and wrist. While absolute agreement between the simulator and measurements was not achieved, the simulator was able to accurately model the variations observed in the channel due to the walking motion. The authors of Mhedhbi et al. [MAAU14] suggest that the discrepancy between the measured and simulated channels can be accounted for due to the trunk shadowing being underestimated by the perturbed ANT model.

In Rosini and D'Errico [RD12a] real-time On-Body channel measurements campaign was performed. At the transmitting side, the measurement test bed was mainly composed by a pulse step generator and a power amplifier, whereas at the receiving side four low noise amplifiers were connected to a digital oscilloscope. This configuration allowed the simultaneous collection of four CIRs, each one corresponding to a different On-body link composed by the i-th TX and the j-th RX. The four receiving ANTs (Rxs) were located on the right and left hand, on the right thigh and on the left ear. Instead,

the device acting as the TX was placed alternatively on the right ear, on the heart and on the left hip position. All the acquisitions were repeated both in anechoic environment and in an indoor office equipped with some general office furniture. In order to account for the human body and movement variability, four human subjects (two males and two females) were involved in the measurements. Each subject performed different movements: still, walking, and standing up, and sitting down from a chair. In order to study the ANT effect on the channel characteristics, all the measurements were repeated with two sets of ANTs: wideband planar monopole (PM) and wideband top loaded monopole (TLM). PMs were placed parallel to the body surface in order to have a main polarisation tangential to the body and they were spaced from it by a 5-mm thick dielectric foam. TLMs, which present good monopolar behaviour, were actually designed to result into a normal polarisation with respect to the body surface.

In Van Roy et al. [VRQL+13], measurement campaign was performed by means of a multiple-input multiple-output (MIMO) 8 × 8 channel sounder. A WBAN consisting of 12 nodes, located over the whole body, as shown in Figure 5.7 was investigated. The positions of the transmit and receive nodes were changed between measurements to get a statistical characterisation of almost all of the 12 × 12. The measurements were taken successively on two male subjects in a quasi-empty room of approximately 5 × 10 m.

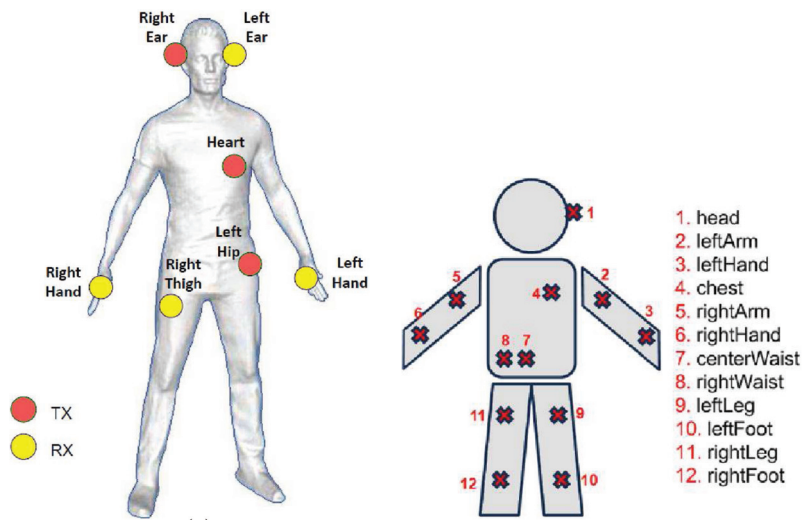


**(a)** **(b)**

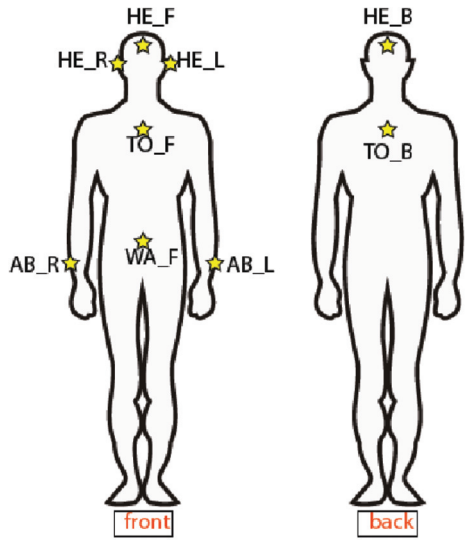


**Figure 5.7** Investigated dynamic on-body channels: (a) Rosini and D'Errico [RD12a], (b) Van Roy et al. [VRQL+13], and (c) Oliveira and Correia [OC13c].

During the measurements, each subject was walking freely around the room. SMT-3TO10MA SkyCross ANTs were employed in two different orienations, respectively, vertically and normally to the body.

In Grosinger and Bosch [GB14], VNA measurements were performed considering different stationary and moving body posutre. Each posture was held 20 s, and the repetition rant of the measurement sas 5 $s^{-1}$, by employing monopoles at 900 MHz and 2.45 GHz.

Besides measurements a simulation approach has been employed in Oliveira et al. [OM12]. The authors exploited FDTD simulation results, using the transient solver of CST MWS, to characterise both static and dynamic on body channels at 2.4 GHz. The tissue electric parameters for the desired frequencies were obtained from the Cole–Cole Model described in [14]. A BAN topology composed of nine wireless nodes distributed over the voxel model in locations that can correspond to a realistic usage scenario was created. In a first study, the body was considered still and patch ANTs were place at different distances from the body (up to 25 cm). Than a realistic model of a female subject in different postures (replicating the body motion from the Poser animation software) was considered [OC13c, OC13a]. Each point of time in the human motion is key framed to create a smooth animation, where

each frame is a 3D object (a posture) exported from Poser into CST. Two typical human day-to-day activities are reproduced, walk and run, each one being a combination of 30 time frames, with 1/30 s duration each.

#### 5.4.2.2 Channel model

For each link under investigation, the time-dependent channel power transfer function in dB, $P_{ij}(t)$, could be computed integrating the channel transfer function, $H_{ij}(t, f)$ over the band of interest $B$:

$$P_{ij}(t) = \frac{1}{B}\int_B |H_{ij}(t,f)|^2\, df = G_{0ij} \cdot S_{ij}(t) \cdot F_{ij}(t). \qquad (5.2)$$

$G_{i,j}$ represents the *mean channel gain,* $S_{i,j}(t)$ is the *long-term fading* or *shadowing* contribution, mainly due to the masking effect of the human body and to its movement. $F_{ij}(t)$ is the *short-term fading* that accounts for the effect of multi-path component (MPC) arising from reflections and diffractions from the environment or from the body itself.

An example of the acquisition performed is shown in Figure 5.8, which presents the evolution over time of $P_{i,j}(t)$ in dB (dashed curves) while the subject is walking in indoor. Each colour refers to one of the on-body link, considering the *TX* placed on the user's left hip.

The comparison between Figure 5.8(a,b) (the latter is equivalent to the former but referring to a static case, where the subject is standing still in the anechoic chamber), highlights how the nodes position and the movement performed affect the dynamic evolution of $P_{i,j}(t)$. This effect particularly emerges when focusing on the slow-varying component of the power transfer function, $S_{i,j}(t)$ (continuous curves). It represents the *shadowing* impact of the body that dynamically masks the direct communication link according the subject movement. For example, following the trend of the continuous blue curve (hip/right hand link), it is possible to retrace the swinging movement of the arm during the walk. The dips of the curve refer to the moments where the arm is behind the subject's torso, i.e., the body completely shadows the communication, resulting in strong channel attenuations. On the opposite, *shadowing* phenomena are quite moderate in static conditions where no movement is performed (Figure 5.8a), and the slight variations of channel $P_{i,j}(t)$ are due to the involuntary breathing of the user.

The complete set of results, which are not reported here for the sake of briefness. In Rosini and D'Errico [RD12a], it was found that PMs generally present smaller values of $G_{i,j}$ as compared to TLMs. This can be explained considering that tangentially polarised ANTs, as PMs are, do not help creeping

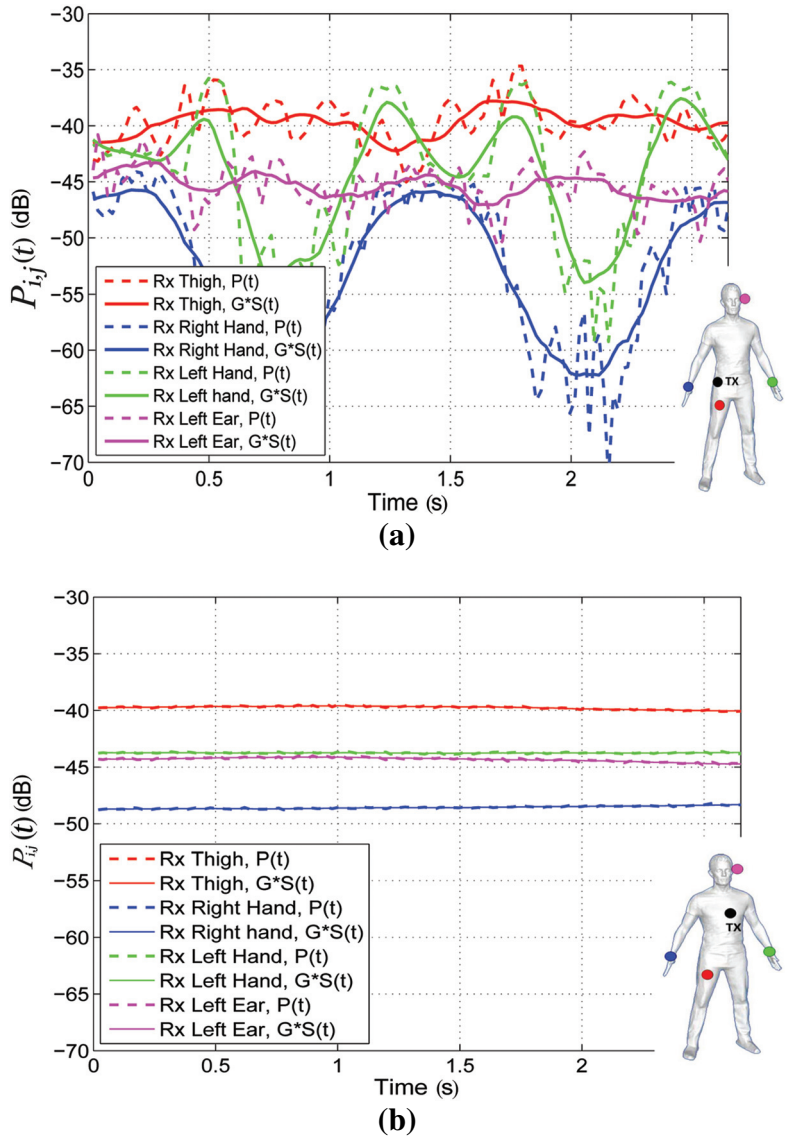


**Figure 5.8** *On-body* channel power transfer functions in indoor: (a) Walking, and (b) Still.

waves propagation on the body, resulting in larger channel attenuations [LHOV09]. As a consequence, this effect is even more evident for the links with a strong on-body propagation component, such as chest/thigh, hip/thigh, or ear/ear.

In classical wireless systems, the *long-term fading* normally accounts for the shadowing effect of some obstacles that obstruct the direct link between nodes. For the specific case of BANs in *On-Body communications*, the definition of *shadowing* describes the condition where the human body itself acts as an obstacle to the main direct transmission path, dynamically evolving according to the movement, as already presented in Figure 5.8. This effect is particularly evident when one of the ANTs is placed on a limb (hand or leg). *Shadowing* values in dB results to be statistically described by a normal distribution, $S_{i,j}(t)|_{dB} \sim N(0, \sigma_S)$, where the standard deviation $\sigma_S$ accounts for the slow variations of $P_{i,j}(t)$ due to the body shadowing effect. Generally, PMs present larger values of $\sigma_S$ as compared to those found for TLMs, meaning that they are more affected by the shadowing effect of the body and by its movement. Indeed, normally polarised ANTs, helping creeping waves propagation around the body, present a dominant main path that overcomes the secondary paths generated by reflections on the body, resulting in a smaller *long-term fading* contribution.

As for the *short-term fading,* $F_{i,j}(t)$, it accounts for the effect of the MPC arising from reflections and reflections on the human body and/or on the surrounding environment. In narrowband, it was found that *short-term fading* is well modelled by a Rice distribution. Normally, polarised ANTs present larger *K* factors as compared to tangentially polarised, meaning that the channel experiments smaller amplitude fading episodes. Higher *K* factors are due to the presence of a main propagation path with stronger energy contribution, which confirms the hypothesis of an on-body creeping wave contribution enhanced by the use of normal polarisation. This difference is particularly relevant for the chest/thigh and chest/ear links, where the propagation happens mostly by on-body creeping waves, and the differences in ANT behaviour due to the ANT effect are even more stressed. Measements in which the user performed dynamic walking on the spot movements in both anechoic and reverberant environments have been exploited in order to address different scenarios and parameters have been extracted in Cotton [Cot15]. One of the main needs for cooperative protocol design is to take into account the space–time correlation properties. In the inter-link correlation properties of two different measurement campaings [PRDO14]. The analysis show that, depending on the walking scenario, the space–time correlation characteristics can vary from very stationary to not stationary at all. For instance, the stationarity cases correspond to the scenarios where the subjects walk uniformly and regularly along a straight line with periodic arm swings, whereas the non-stationary behaviour arises from random trajectories and

irregular arm swings. In Oliveira and Correia [OC13d], the movement was generated by an animation software, using a realistic shaped homogeneous phantom, to investigate the inter-link correlation and power distribution, when the body is moving. Results shown that the movement decreases the correlation between the branches to values below 0.7. With respect to the targets for MIMO (correlation and imbalance below 0.7 and 10 dB, respectively), the running environment has 29% of its samples inside the target area, against 34% for the walk scenario. In particular, TXs on the ears are the ones with more links satisfying the minimum MIMO requirements [OC13b]. In order to reproduce the space–time correlation characteristics in walking scenario, an auto regressive model for long-term and short-term fading has been propsed along with a Matlab implementation [ARD14].

## 5.5 Off-Body Radio Channel

*Off-body* communications take place between at least one node *on* a human body and another one *outside* it, either worn by another user (*B2B* case) or acting as a static external gateway (*on-to-off body* scenario). Off-body communications have been just recently approached, with a limited number of contributions available in literature [ACS09, CS07, CS09, HMS+10, GBS08, KAY10, MPS+14a, RD12c, RVD14, SHJ+09, WBN+09, ZCSE04], mainly dealing with the *on-to-off body* case [Ros14]. In order to characterise this type of channels, specific investigations are needed, and a great effort has been done by the TWGB in this direction. Several TDs focused on the modelling of transmission channel's main components (i.e., distance-dependent mean PL, shadowing and fast fading), accounting for the dynamics of human movement and ANT/body joint effect. Both simulations and experimental approaches were adopted, covering not just the ISM band at 2.45 GHz, but also the UWB and the 60 GHz one. Moreover, some works studied link correlation properties, to be exploited in the perspective of realising MIMO configurations.

### 5.5.1 On-to-Off Body Channel Characterisation

The body presence on one side of the radio link significantly affects ANT's radiation properties [MC13]. Body movements result in time-varying propagation characteristics and variations of ANT's orientation (i.e., maximum radiation direction), which influence the overall channel. The authors Mackowiak and Correia [MC13] investigated the statistical behaviour of ANT's radiation pattern in dynamic conditions. Based on the description of

the variation of the normal to the body surface during motion, a statistical characterisation of the changes in ANTs' radiation pattern (i.e., patch ANT at 2.45 GHz [MC06]) is provided. Considering that the influence of body dynamics on ANT's orientation depends on its on-body location, different node positions were taken. Simulation results show that when ANTs are placed in very dynamic body segments the standard deviation of the normal to the body surface is very large; the radiation pattern shape gets more uniform compared to the static case, and its standard deviation is also very high in all directions [MC13].

#### 5.5.1.1 Channel modelling at 2.45 GHz

The work by Mackowiak and Correia [MC12] proposes the integration of the ANT statistical model in Mackowiak and Correia [MC13] with the description of the propagation environment, to develop a flexible simulation platform for modelling on-to-off body channels. Simulations were run for a human subject carrying four on-body nodes (patch ANT operating at 2.45 GHz) located on different positions, who moves along a street in front of an external isotropic device placed at 3 m height. The channel is characterised in terms of received power, delay spread, and direction-of-arrival (DoA). Propagation conditions are classified as *LoS, NLoS*, or *Mix*, according to the mutual position of on-body and outer devices. Results show that channel parameters depend on body movement, ANT position, and distance between devices. For instance, Figure 5.9 compares the evolution of the average received power while walking and running, considering four different situations: front side of the head ($HE_F$), left and right arms at wrists ($AB_L$ and $AB_R$), and back side of the torso ($TO_B$). In the latter case, propagation conditions for the left arm node change rapidly from LoS to NLoS, resulting in deep fades. Moreover, arms present symmetric trends regarding the position of the outer ANT, while forehead and back nodes show similar values of the received power, but at opposite ends of the path [MC12].

Starting from Mackowiak and Correia [MC12], the same authors [Mc14] propose a PL model for dynamic on-to-off body channels. The model is given in terms of total PL as $L_{\mathrm{PT}}(d)_{[dB]} = \Delta L_{\mathrm{P}}(d)_{[dB]} + \Delta L_{\mathrm{B}[dB]} + \Delta L_{\mathrm{F}[dB]}$, where the mean PL, $L_{\mathrm{P}}(d)_{[dB]}$, is characterised by a log-distance linear fit of the channel values obtained for different body positions and orientations; $\Delta L_{\mathrm{B}[dB]}$ is a random variable modelling the body shadowing; while $\Delta L_{\mathrm{F}[dB]}$ accounts for the influence of the propagation environment describing the fast fading component. Simulations are run for a BAN at 2.45 GHz, with eight on-body patch ANTs carried by an user who changes position in an indoor

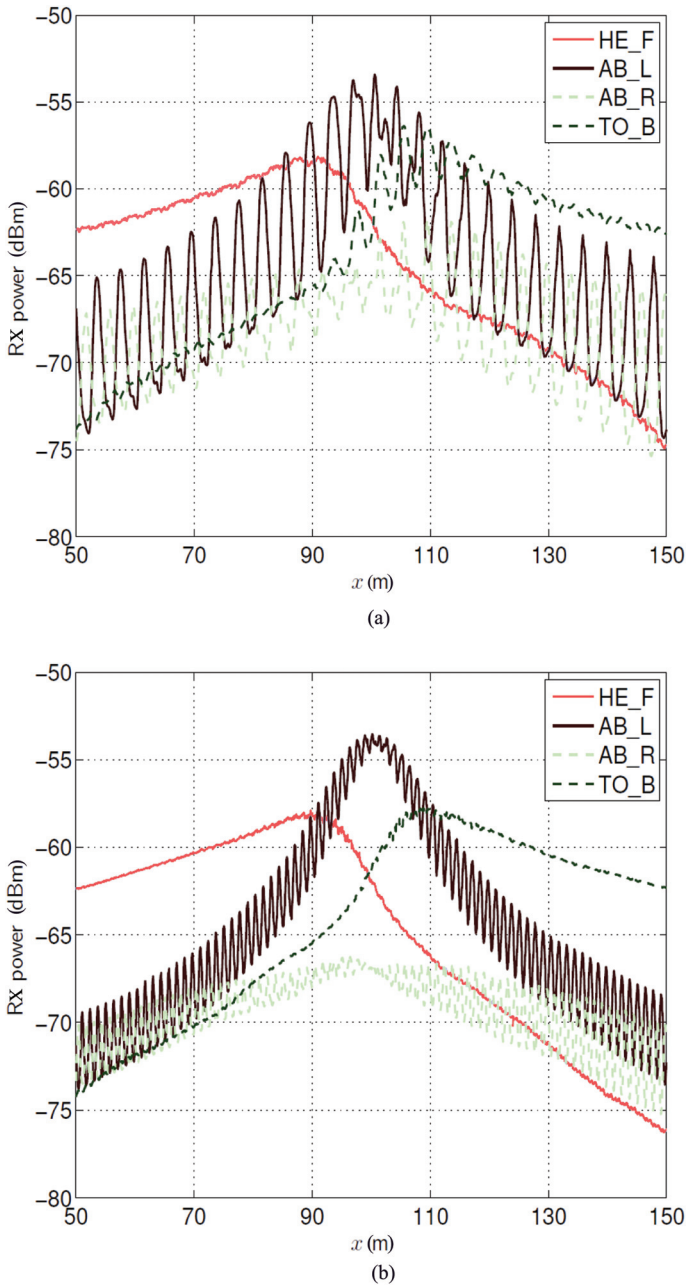


**Figure 5.9** Average received power when a person is moving along a street [MC12]. (a) Walking, and (b) Running.

environment [MC14]. PL results dependent on the propagation conditions, with higher values in NLoS than in LoS. The fading amplitude is statistically modelled by a Nakagami distribution. As for the body shadowing, it is a dominant component in the CM, since the body can act as an obstacle to the direct communication link during movement, resulting in an additional attenuation to the mean PL.

Body shadowing characterisation is also the focus of Aoyagi et al. [AKT14, ATK14a, ATK15]. Simulations estimate the occurrences of shadowing (i.e., passage from LoS to NLoS), which depend on the movement type and the angle of the wave incidence on the body, according to nodes' mutual position [ATK14a]. Shadowing rate is modelled through a sigmoid or a normal distribution, considering the azimuth angle of the incident wave as the fitting parameter. Here, the shadowing rate means the probability of shadowing occurrence for a specific incident angle during motion. It is included in a closed formulation for the on-to-off body channel characterisation, to account for the body shadowing effect [AKT14, ATK15]. The effectiveness of the on-body node location is evaluated through the LoS ratio $R^n$, defined as the total number of LoS occurrences over the total number on LoS/NLoS ones. The head node gets the highest $R^n$, since it is less shadowed by the body and hence more often in direct visibility with the external device.

A channel modelling approach similar to the one in Mackowiak and Correia [MC14] is proposed in Rosini and D'Errico [RD12c], but based on experimental channel data. Measurements at 2.45 GHz were performed in anechoic and indoor environments, with one user carrying three on-body nodes. Both static and dynamic conditions were reproduced, with the user facing or giving his back to the outer device (i.e., LoS and NLoS case). Two set of ANTs with different polarisations relative to the body surface [RD12b] are used, to account for the ANT impact on channel characteristics. The model identifies two main components: a log-distance dependence and a fading contribution. The channel gain depends on body orientation, ANT type and on-body position, as shown in Figure 5.10 for measurements in standing LoS conditions in an anechoic chamber. Each colour refers to a specific node position. Generally, channel gain is smaller in NLoS with negligible distance dependence, due to the presence of the body shadowing the direct communication path [RD12c]. The body shadowing is also described as an additional loss contribution to the channel gain in LoS, given as a function of body orientation. The fading component accounts for the environment and motion effect, and its envelope is statistically characterised by a Nagakami distribution.

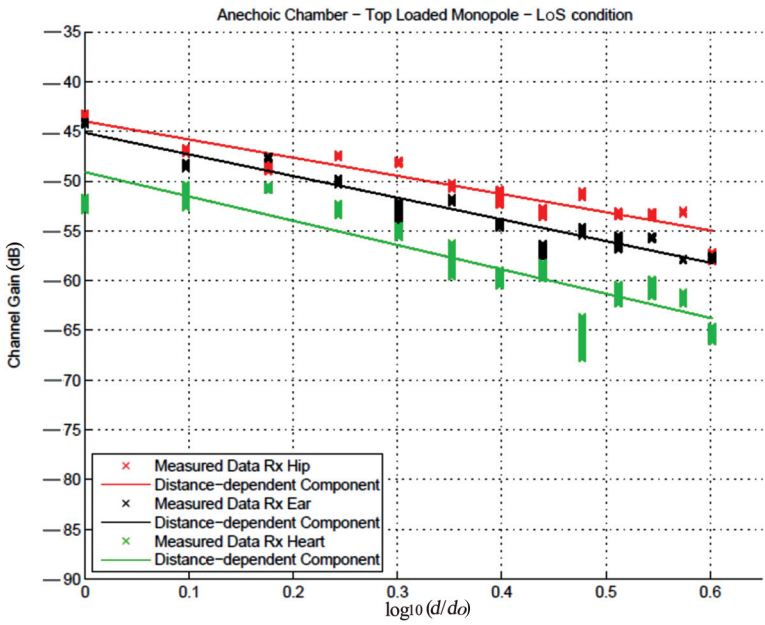


**Figure 5.10** Channel gains for on-to-off body channels [RD12c].

Another experimental indoor off-body PL model at 2.45 GHz is derived in Ambroziak et al. [ARLM14]. Here, measurements are performed in both static and dynamic conditions with two users carrying three on-body patch ANTs. Acquisitions were repeated varying body orientation and for increasing distances from the external device (i.e., a dual polarised ANT). In accordance to the consideration drawn in Rosini and D'Errico [RD12c], results shows the strong influence of ANT on-body location, body orientation, and its PHY characteristics on PL and its distance dependence. The analysis of dynamic scenarios reveals also a great variability of PL values due to movement, when body shadowing episodes may take place, resulting in significant attenuation of the channel.

Paper of Mackowiak et al. [MRDC13] compares the results for the CM presented in Rosini and D'Errico [RD12c] with simulation ones obtained from Mackowiak and Correia [MC12, MC14]. The reference scenario includes indoor and anechoic environments, where an user walks towards/backwards an external device, carrying three on-body nodes [RD12b]. The comparison of the PL values shows a good agreement for both the anechoic and indoor case. An example is shown in Figure 5.11 for the head node, where PL values are given as a function of the distance from the external device. Curves follow the

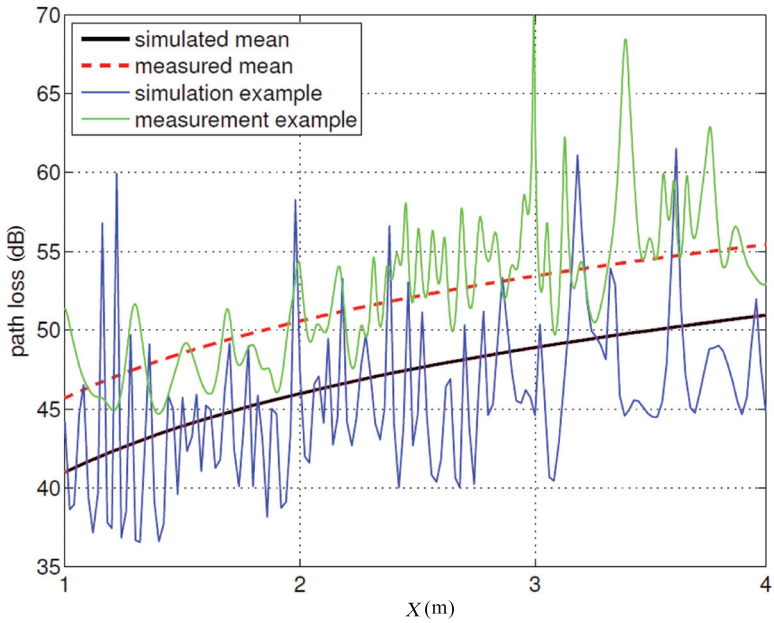


**Figure 5.11** PL for the head node, indoor scenario [MRDC13].

same trend, and the gap can be due to differences in the simulated environment, exact node position and movement performed in the two cases. Moreover, the polarisation effect is not considered during simulations, while it is inherently included in measurements [MRDC13].

Another work comparing simulations and measurements is presented in Ambroziak et al. [AMS+14]. The validation of the PL model described in Mackowiak and Correia [MC14] is obtained using the channel data acquired as described in Mackowiak et al. [ARLM], considering a dual polarised ANT as the outer device. Results show a good agreement between measurements and simulations, even if some deviations are found especially in NLoS, due to ANT's depolarisation effect not modelled in simulations [AMS+14]. The same set of measurements is used in Ambroziak et al. [ARLM14] to study the depolarisation of radio wave propagation in indoor on-to-off body communications, which is mainly due to the presence of the MPCs generated by reflections and diffractions from the surroundings. The metric used in the analysis is a ratio between the power received by the vertically and the horizontally polarised outer ANT. A positive ratio means a stronger vertical component, which is desirable for on-to-off body communications [CLV98]. This parameter is extremely affected by node on-body position and user

orientation, and the highest values are observed when the on-body ANT is co-directed with respect to the external one.

#### 5.5.1.2 Channel modelling at other frequency bands

ISM is one of the possible frequency band for BAN operations, since it is worldwide available and licence free. The main drawback is that other existing communication standards are defined in the same bandwidth (e.g. IEEE802.15.4/ZigBee [IEEE06], and Bluetooth [blu10]), and coexistence issues may arise. To overcome these problems, other bands are proposed, among them UWB being a very promising alternative. The authors Pasquero and Errico. [PD14] present an experimental UWB on-to-off body indoor CM, in presence/absence of the human body. Measurements are performed by placing some UWB dipoles in different positions on a standardised human-like phantom, varying its orientation and distance relative to the outer device. Angles of arrivals and clusters are estimated via the SAGE [VRLO$^+$09] and K-means algorithms [HTK06]. Results show that shadowing from the body has a strong impact not only on the PL, but also on angle of arrival and cluster distribution, due to the higher directivity of the ANT when on-body. Cluster centroids and dispersions are modelled as a function of the body orientation and the distance separating the on- and off-body devices. To complete the model, the dense MPCs component is also characterised [PD14].

The unlicensed 60 GHz band is also proposed for BAN applications for its high data rates. Paper by Mavridis et al. [MPS$^+$14b] presents an indoor CM derived from the solution of the scattering of a plane wave on a cylinder at 60 GHz, the latter representing the human body. The scattering model is composed of two parts (i.e., the solution in the lit and the shadow region) and it is validated through some experiments with a real human body. To include the impact of the environment, authors consider the IEEE802.11ad 60 GHz indoor CM [IEEE12a] and find a mathematical operator that allows the conversion from that model to an on-to-off body one. It is shown that this operator depends on the radius of the cylinder, and on the polar coordinates of the on-body ANT relative to the outer device [MPS$^+$14b].

#### 5.5.1.3 Channel correlation properties and MIMO systems

Body area network performances are generally affected by the environment, body dynamics and posture, and ANT characteristics [MTT$^+$13]. One solution to improve network reliability is the use of Virtual MIMO configuration as multi-ANT systems. Indeed, ANT diversity helps in overcoming the MPC propagation of the signal, increasing the robustness of the system [MTT$^+$13].

A condition to exploit ANT diversity is the link independence, which can be measured by the correlation level among them and is related to radio propagation conditions [ML12]. Starting from the channel modelling approach by Mackowiak and Correia [MC12], Mackowiak and Correia [ML12] presents the results on the evaluation of the correlation between nine off-body links. The average correlation and standard deviation are calculated for all possible link combinations, results being presented in Figure 5.12. The highest correlation is found for co-directed ANTs (i.e., placed on the same side of the body), while the lowest (providing the best diversity) for opposite-directed ANTs (i.e., opposite sides). As for correlation's standard deviation, the largest values are for highly dynamic scenarios. These results helps in the definition of the optimal position for on-body ANTs in terms of diversity and decorrelation. To complete the model, paper of Mackowiak and Correia [ML13] analyses the capacity of a $2 \times 2$ MIMO system, starting from the same simulation scenario considered in [ML12], looking for the optimal node configurations maximising overall system performance. For the reference scenario, the pair of nodes located on the left side of the head and left arm realise the largest capacity gain, with 67% more data transmitted relative to a single-input single-output (SISO) configuration. The main reason is due to good propagation conditions during body movement, and low power imbalance [ML13].

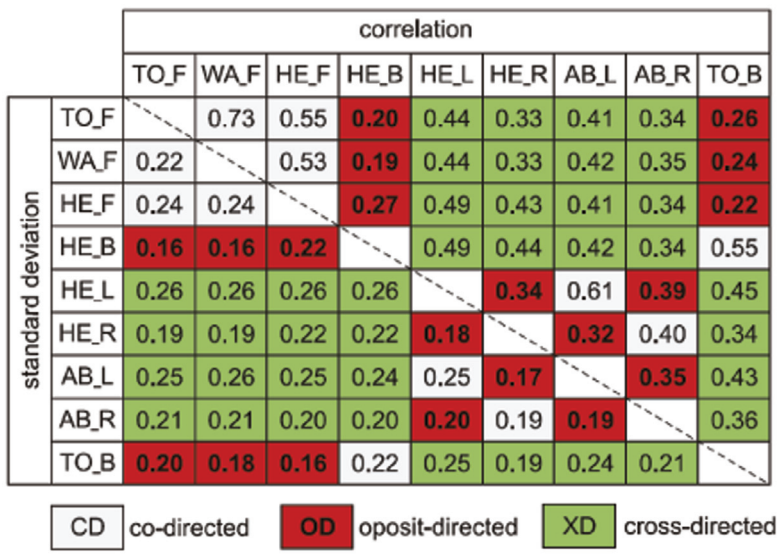


**Figure 5.12** Correlation average and standard deviation [ML12].

Correlation properties are also investigated in Rosini and D'Errico [RD13], starting from channel data acquired as described in Rosini and D'Errico [RD12c]. Links correlation is evaluated as the cross-correlation between the fading contributions of the channels, which is influenced by ANT's characteristics and measurement conditions. For instance, correlation levels in LoS strongly depend on on-body location, while this effect is reduced when in NLoS, due to the masking effect of the body [RD13]. Channels coherence over time is studied as its time correlation and is computed as the normalised autocorrelation function. ANT type and measurement conditions have a strong impact also on this parameter. In particular, moving from LoS to NLoS implies a faster decorrelation, and autocorrelation functions present a less smoother evolution, due to the stronger MPCs that makes the channel less stable over time [RD13].

The authors in Marinova et al. [MTT+13] propose a method for determining the minimum number of ANTs to be used in an UWB MIMO configuration in order to provide low correlation, hence higher diversity. Electromagnetic fields around a human body are generated for three sampled frequency representing the whole UWB (i.e., 3.1, 6.85, and 10.6 GHz). To solve this optimisation problem, the authors assume that if a combination of $n$ ANT positions is optimal, then the same combination is used to find the next position for an optimal $n + 1$ configuration [MTT+13]. Once the positions are identified, simulations are run including ANT characteristics mounted on a human body phantom, and new correlation and diversity matrix are evaluated. Results are compared with those obtained for randomly positioned ANTs or a set of most commonly used on-body locations, as shown in Figure 5.13. The proposed methods generally achieves the best results, while the most common positions solution is the worst one, proving the need for an alternative method to chose the optimal ANT configuration.

### 5.5.2 B2B Channel

A limited number of contributions in literature focus on B2B communications, and just few of them propose a precise radio channel characterisation. Papers by Rosini et al. [RDV12, RVD14] present an experimental modelling of the B2B channel based on indoor measurements at 2.45 GHz. Two couples of subjects carrying some nodes placed on several locations and performing different type of movements are involved. To account for ANT's effect, measurements are repeated with two sets of ANTs. Similar to Rosini and D'Errico [RD12c], the channel is modelled through a mean channel gain

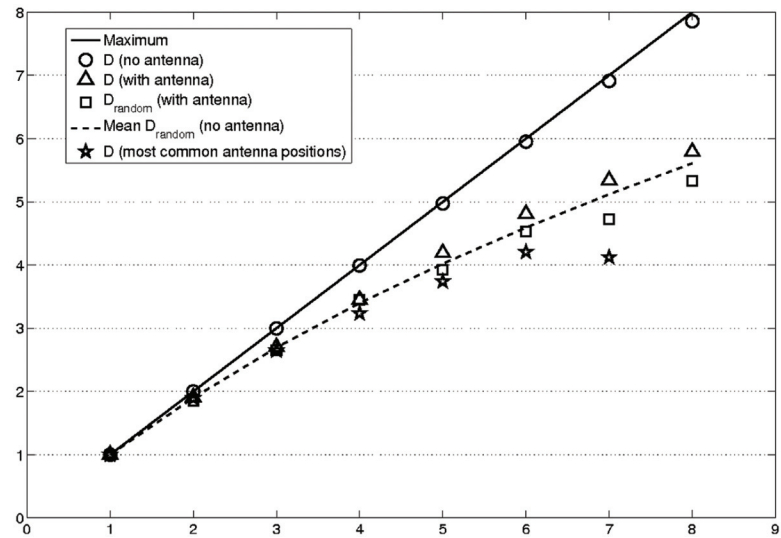


**Figure 5.13** Diversity for different nodes configurations [MTT+13].

and a fading contributions. The mean gain is characterised as a log-distance dependent component, defined by the PL exponent and its value at the reference distance of 1 m. Results show that it depends on the node position and ANT type. The linear envelope of the fading component, accounting for the MPCs from the moving body and the environment, is described by a Nakagami distribution [RDV12].

The body shadowing effect is also characterised; it extracted from the channel power transfer function following the slow variations of the channel gain over its mean value, and it is accounted for as an additional loss contribution as a function of subject orientation [RVD14]. The distribution of shadowing values takes a two-lobe configuration, which is modelled using a mixture distribution composed of two gaussian distributions [RVD14].

Different type of movements result in specific effects on channel time-variant characteristics. For instance, Figure 5.14 shows the different evolution of the channel power transfer functions for the case of the two subjects walking side by side and when one of them walks towards the other. In the first case the oscillating trend of curves is due to the subjects' hand that cyclically masks the direct communication link (nodes are on both subjects' hip) while walking; while in the second scenario the curves smoothly decrease as the distance between users increases, presenting neither periodic behaviour nor strong supplementary attenuations, since nodes are always in LoS conditions.

## 5.6 MAC Protcols and Upper Layers

The peculiarities of BAN propagation channel, arising from the body presence, can impact the design of MAC and upper layer communication protocols. Network reliability and energy efficiency are among the most critical requirements [BSM+12] to be met, and common solutions used in generic wireless sensor networks (WSNs) may not be appropriate for *body-centric communications* [CGV+11]. Moreover, considering the proposed ISM operational frequency band at 2.45 GHz, BANs are expected to coexist with other co-located ISM-based wireless devices. As such, interference from coexisting wireless systems (e.g. Blutooth, ZigBee, and Wi-Fi) or even other nearby BANs could degrade the reliability of BAN communications [ABSV13]. A precise characterisation of interfering sources, and the evaluation of achievable performance for multiple BANs, is hence of outmost importance for the design of appropriate interference mitigation and management techniques [Ros14].

### 5.6.1 MAC Protocols for BANs

The wide variety of applications for BANs imposes a set of system requirements that none of the existing air interfaces are able to meet Rosini et al. [RMM+12]. As a result, the IEEE802.15.6 group was established to develop a standard (released in 2012) optimised for short-range communication in the vicinity of, or inside, the human body [IEEE12b]. A description of standard's main features, particularly those related to the medium access control (MAC) layer, can be found in Cavallari and Buratti and Subramani et al. [CB14, SCS13]. Performance of random and scheduled access in terms of packet drop, latency, packet delivery ratio (PDR) and reception occurrences for different data rates and transmit powers is evaluated and compared in Subramani et al. [SCS13]. Considering just the beacon access mode with superframe (SF) boundaries, authors Cavallari and Buratti [CB14] propose an analytical model to characterise the performance of IEEE802.15.6 carrier sense multiple access with collision avoidance (CSMA/CA), where nodes are assigned a different priority to access the medium according to the traffic type. Network performance is evaluated in terms of packet reception success probability, and no retransmission is allowed. The model is validated through experiments. This study can provide information on the expected performance of these networks, as well as criteria to optimise the assignment of node priorities [CB14].

Apart from IEEE802.15.6, other standards such as IEEE802.15.4 [IEEE06] and Bluetooth [blu10] are also considered for BANs communications. In particular, authors in Rosini et al. [RMM+12] present simulation

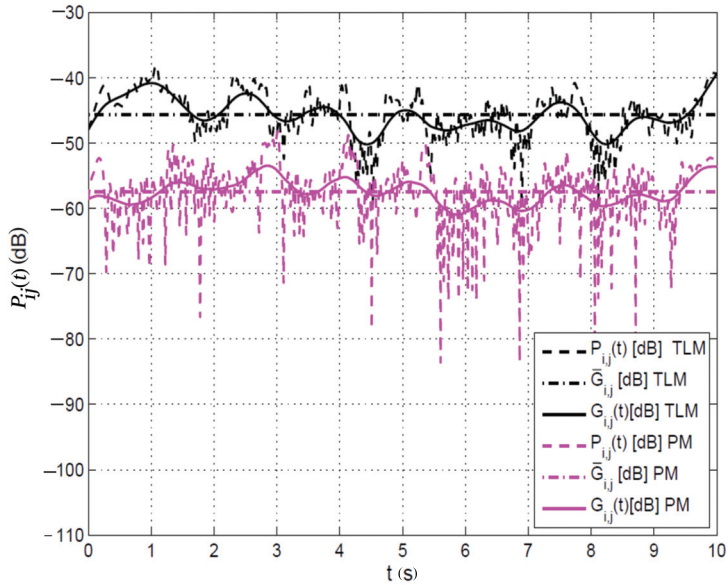


**(a)**

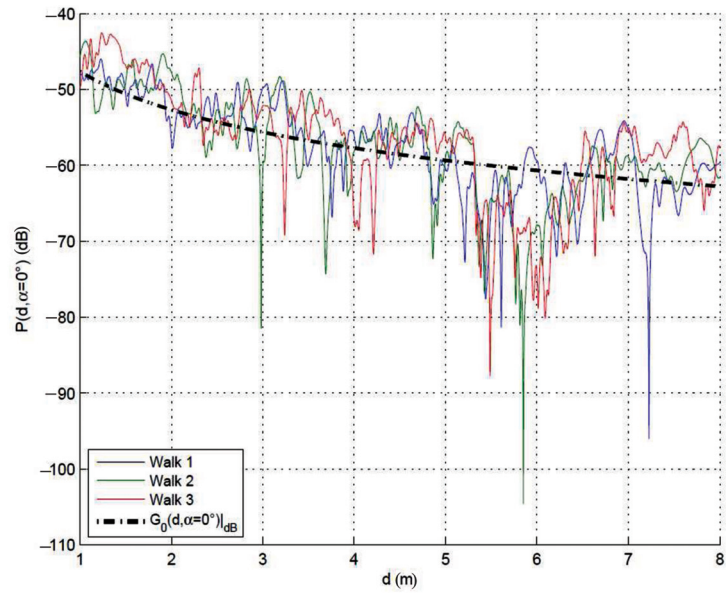


**(b)**

**Figure 5.14** Channel gains for different movements [RVD14, RDV12] (a) Walking side by side, and (b) One subject walking towards the other.

results comparing the performance of two CSMA/CA protocols (as defined by the IEEE802.15.4 and 802.15.6 standards), and the IEEE802.15.6 Slotted Aloha algorithm, combined with three PHY layer solutions. The performance metrics considered are packet loss rate (PLR), average delay, and energy consumption. To account for realistic propagation conditions, real-time dynamic channel measurements obtained for two sets of ANT are included in the simulations [RD12c]. Figure 5.15 shows a sample of the results (i.e., PLR as a function of the packet payload); it is generally quite difficult to identify the best performing MAC, as the ANT type, the underlying PHY and the considered metric can greatly impact the outcome. For this reason, flexible protocols should be designed in order to adapt to different applications requirements. The results from Rosini et al. [RMM+12] could serve as guidelines for the selection of the best protocol given a specific application.

Energy consumption, which is one of the critical issues in BANs, is the focus of Maman et al. [MDPRD12]. A well-designed communication scheme managed by an efficient MAC protocol can minimise the energy consumption of these networks. Authors in Maman et al. [MDPRD12] present

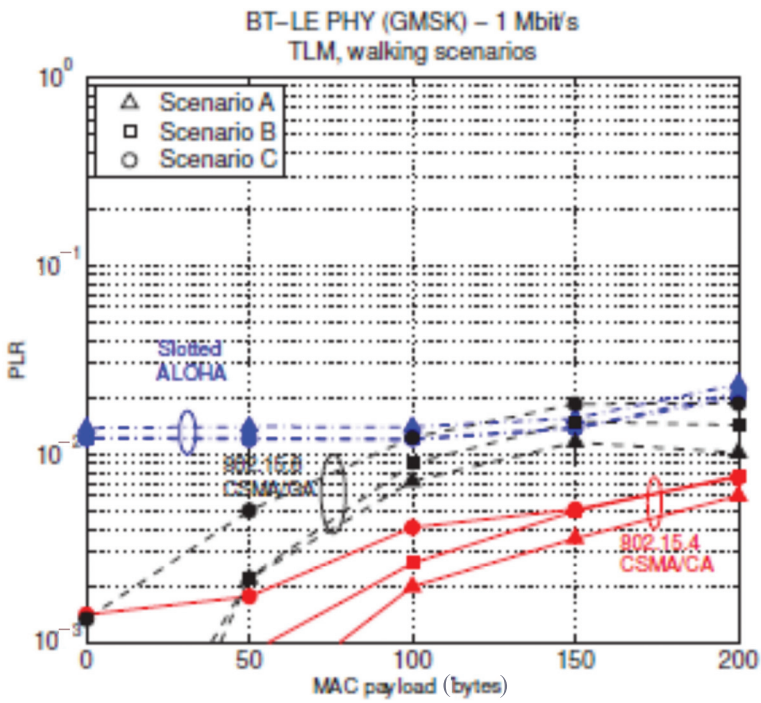


**Figure 5.15** Average PLR for different MAC protocols, bluetooth-low energy (BLE) PHY.

the performance study of dynamic relaying and cooperative routing schemes to ensure energy efficiency. Simulations are run considering a coordinator node located on the hip and three potential relays on the wrist, shoulder and thigh. The MAC protocol considered (i.e., BATMAC [MO11]) uses the beacon packet error rate (PER) information in order to efficiently manage the cooperative relay mechanism. Packet reception decision is then based on PER value, which itself depends on the instantaneous signal-to-noise ratio (SNR) [DRM11]. Several relaying mechanisms based on beacon reception feedback are proposed and compared with the objective of ensuring energy efficiency, low latency and high data delivery ratio. Energy consumption levels are evaluated considering the characteristics of on-the-shelf Bluetooth-compliant devices. Both for an ideal case (i.e., stationary channel) and more realistic conditions (i.e., accounting for the impact of fast fading), the mix strategy proposed in Maman et al. [MDPRD12] provides the most efficient trade-off between energy consumption and reliability.

### 5.6.2 Interference Management and Coexistence Issues in BANs

One of the frequency bands envisaged for BAN operation is the 2.45 GHz ISM band. Considering that several existing communication standards such as Wi-Fi, Zigbee, and Bluetooth work in the same band, interference with such systems may take place and needs to be characterised. To that purpose, authors Martelli and Verdone [MV12] study some of these coexistence issues to evaluate the performance of a BAN operating in presence of nearby wireless devices working with IEEE802.11 (Wi-Fi) [IEEE11] and IEEE802.15.4 [IEEE06] protocols. Three modulation schemes at the PHY along with two CSMA/CA algorithms at the MAC layer are considered for performance evaluation [RMM+12]. Simulations are set up for a human subject wearing a BAN and walking in a room, while either a Wi-Fi AP and a notebook or a Zigbee network is active. BAN performance is assessed in terms of PLR, average delay and average TP as a function of the packet payload. Numerical results show that independent from the considered PHY/MAC solution, the PLR is the parameter mainly affected by the presence of interference, in particular when coexisting Wi-Fi systems are working. Therefore, to guarantee an acceptable level of performance, a dynamic selection of BAN operating channels could be extremely important [MV12].

As there are currently no coordinating mechanisms among multiple co-located BANs, co-channel interference from transmissions in adjacent BANs could impact the reliability and the QoS experienced by a node within an individual BAN. Authors in Alasti et al. [ABSV13] develop a flexible

simulation platform that allows for statistical evaluation of interference in multi-BAN scenarios and performance of possible mitigation algorithms. The platform consists of a virtual room with variable number of BANs, moving around according to a defined motion scenario. Assuming a time division multiple access (TDMA) transmission protocol, several uncoordinated slot assignment strategies are proposed in Alasti et al. [ABSV13, BSA15] to mitigate inter-BAN interference. The best strategy, referred to as *"Minimum Required SINR Assignment"*, tries to re-allocate the slot assignment according to a protocol shown in Figure 5.16. Exploiting channel correlations and based on the experienced interference in the current frame, the protocol identifies the timeslots (i.e., those with SINR above the required minimum) that are least likely to collide with other BAN interferers in the next frame. The improvements in the experienced signal-to-interference ratio (SIR) and link

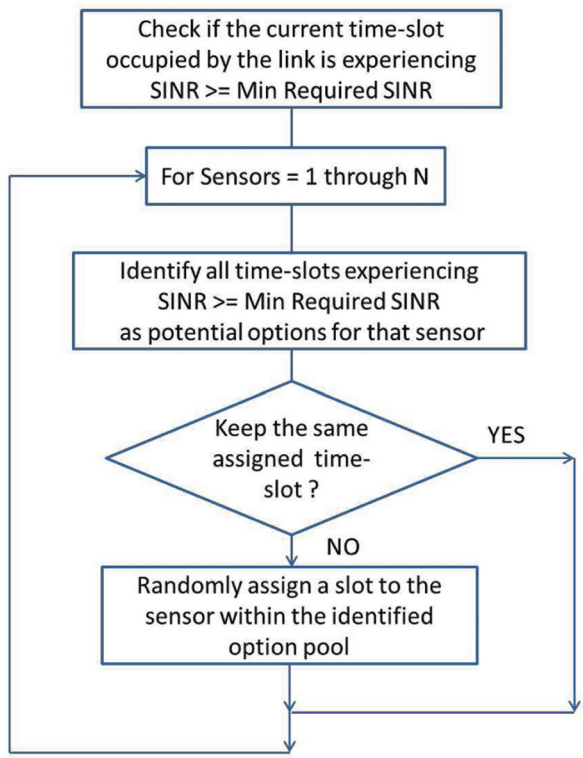


**Figure 5.16** *"Minimum required SINR assignment"* strategy.

outage probability show the effectiveness of such uncoordinated mitigation strategies for several motion scenarios.

For off-body communication in dense BANs environment, authors in Mijovic et al. [MBZV14] propose cooperative transmissions to enhance link quality. It is assumed that the nodes of a BAN can cooperate and form a virtual ANT array (VAA) in order to transmit data to one of the sinks in an indoor environment. The latter are equipped with multiple ANTs, hence, a MIMO system can be established. Using beamforming, the ANT elements on both RX and TX sides set their weight coefficients as to enhance the received signal. Several scheduling techniques that sinks may adopt to optimise various performance metrics (e.g., block error rate (BLER), SNR, and Jain index) are considered. Simulation results show the advantages of cooperative beamforming in terms of SNR and BLER, over traditional SISO systems [MBZV14].

## 5.7 CM Parameters

In this section, we report the main parameters of the CM developed in the frame-work of the TWGB of IC1004 action. For the model explanation, the reader can refer to the previous sections and the references reported. CM parameters are derived from different measurement campaigns, involving different human subjects, ANTs and environments. For this reason some simplifications and merging of results were needed.

The on-body CM is derived for UWB and narrowband 2.4 GHz communications. The parameters here reported mainly refer to dynamic conditions, i.e., to walking scenarios. In UWB the results are reported for dipole and loop ANTs. At 2.4 GHz the results depend on the orientation of the ANT main polarisation orientation with respect to the body surface (i.e normal or tangential). Nodes naming are detailed in Figure 5.17. All the parameters avaialble, e.g. the space-time correlation properties, are not reported here for the sake of briefness, but Matlab implementations have been developed [ARD14].

For the off-body channel, node-specific parameters have been extracted (see Section 5.5). However here the basic idea is to extract a model able to account for the main aspects affecting channel characteristics and that are related to devices spatial diversity. For this reason the human body was partitioned in three areas, namely *Head, Upper Body,* and *Lower Body,* as shown in Figure 5.17. The *Head* part is composed of the whole skull and the neck. In practice the results here consider an ANT placed on the righ ear. It should be noted that for the *Head* part the proposed model applies to the case

| Name | Position |
|---|---|
| LE | Left Ear |
| RE | Right Ear |
| LE | Left Elbow |
| RE | Right Elbow |
| LC | Left Chest |
| FC | Front Chest |
| RC | Right Chest |
| LHi | Left Hip |
| FHi | Front Hip |
| RHi | Right Hip |
| LTi | Left Tight |
| RTi | Right Tight |
| LK | Left Knee |
| RK | Right Knee |
| LF | Left Foot (Ankle) |
| RF | Right Foot (Ankle) |

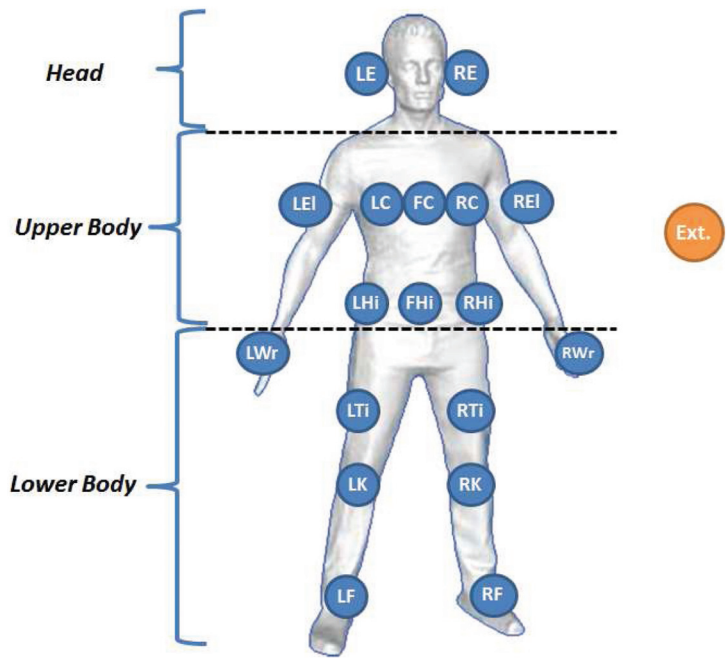


**Figure 5.17** Nodes position, and body partitioning for *off-body* CM considerations.

where nodes are placed on user's ears, face, neck or back of the neck. Whean a node is placed on the top of the head, a classical indoor CM can apply, since there is no shadowing from the body. The *Upper Body* is the portion of the body included between the shoulders and the hip, plus the upper part of the harms, whereas *Lower Body* refers to the lower section of the body including feet and hands, hence the most mobile part of the body. The focus of this CM is on body dynamics and particulalry on walking conditions. When possible ANT topology-dependent parameters are given.

### 5.7.1 On-Body CM

#### 5.7.1.1 Dynamic UWB on-body channel

In this subsection, we report the fading parameters for the UWB on-body channel, focusing on the static and dynamic, i.e., walking condition. For channel gain parameters the reader can refer to references in Section 5.4.1. The parameters refer to different distributions. The PDF of the Weibull, Lognormal and Gaussian distributions are:

$$f(x|a,b) = \frac{b}{a}\left(\frac{x}{a}\right)^{b-1} \exp\left[-\left(\frac{x}{a}\right)^{b}\right],\ x > 0 \tag{5.3}$$

$$f(x|\mu,\sigma) = \frac{1}{x\sigma\sqrt{2\pi}} \exp\left[\frac{-(\mathrm{In}\ x - \mu)}{2\sigma^2}\right],\ x > 0, \tag{5.4}$$

$$f(x|\alpha,\beta) = \sqrt{\frac{\beta}{2\pi x^3}} \exp\left[-\frac{\beta}{2\alpha^2 x}(x-\alpha)^2\right],\ x > 0, \tag{5.5}$$

#### 5.7.1.2 Dynamic on-body channel at 2.4 GHz

In this section, we report the On-Body CM parameters according to the description given in Section 5.4.2. The model is based on the separation of the *mean Channel Gain*, charaterised by its mean value $\mu_0$ and the standard deviation $\sigma_0$, taking into account the human body variability. The *long-term fading* (or shadowing) is normmally distributed in dB (standard deviation $\sigma_s$), while the *short-term fading* follows a Rice distribution characterised by its *K* factor. The space–time correlation properties are not reported here, but can be found in Pasquero et al., Oliveira and Correia, and Arnesano et al., [PRDO14, OC13d, ARD14]. (Tables 5.3 and 5.4)

### 5.7.2 Off-Body CM

The proposed off-body radio CM describes the *off-body* channel power transfer function in *dB*, *P* (*d*, $\alpha$), as a function of the distance *d* between devices

**Table 5.3** CM parameters: normal polarisation

| | | | Channel Gain | | Shadowing | Fading |
|---|---|---|---|---|---|---|
| | Position 1 | Position 2 | $\mu_0$ (dB) | $\sigma_0$ (dB) | $\sigma_s$ (dB) | $K$ |
| Anechoic | LHi | RTi | −38.78 | 2.06 | 1.43 | 41.32 |
| | LHi | RWr | −52.09 | 4.58 | 4.05 | 15.43 |
| | LHi | LWr | −40.32 | 3.17 | 3.73 | 15.43 |
| | LHi | LE | −47.24 | 2.02 | 1.35 | 114.78 |
| | LHi | RF | −63.26 | 5.13 | 2.03 | 2.73 |
| | LHi | RC | −45.95 | 1.44 | 0.88 | 33.65 |
| | LHi | REl | −58.28 | 5.79 | 4.11 | 9.27 |
| | LHi | RE | −73.10 | 6.37 | 4.34 | 3.79 |
| | LHi | RK | −57.44 | 5.17 | 3.24 | 3.45 |
| | LHi | Rhi | −46.82 | 2.33 | 1.32 | 15.17 |
| | LHi | RWr | −59.69 | 6.16 | 3.09 | 1.09 |
| | FC | RTi | −38.45 | 1.06 | 1.07 | 130.07 |
| | FC | RWr | −47.07 | 2.16 | 3.46 | 130.07 |
| | FC | LWr | −43.86 | 2.46 | 3.67 | 122.07 |
| | FC | LE | −48.62 | 3.62 | 1.06 | 171.47 |
| | RE | RTi | −55.13 | 3.29 | 4.06 | 25.51 |
| | RE | RWr | −53.82 | 3.92 | 2.25 | 105.02 |
| | RE | LWr | −66.59 | 4.98 | 2.53 | 30.18 |
| | RE | LE | −35.81 | 0.82 | 0.12 | 8433.13 |
| Indoor | LHi | RTi | −38.4 | 1.17 | 1.01 | 29.59 |
| | LHi | RWr | −53.09 | 2.89 | 3.98 | 5.83 |
| | LHi | LWr | −40.74 | 4.32 | 3.45 | 6.72 |
| | LHi | LE | −48.3 | 2.69 | 2.79 | 10.33 |
| | FC | RTi | −38.65 | 1.15 | 1.4 | 69.75 |
| | FC | RWr | −49.47 | 1.2 | 2.57 | 21.97 |
| | FC | LWr | −42.97 | 3.19 | 1.97 | 54.67 |
| | FC | LE | −46.82 | 4.57 | 1.5 | 17.34 |
| | RE | RTi | −57.57 | 1.84 | 3.17 | 1.44 |
| | RE | RWr | −53.31 | 3.19 | 2.89 | 7.40 |
| | RE | LWr | −57.57 | 0.91 | 1.72 | 0.00 |
| | RE | LE | −37.01 | 2 | 0.67 | 50.00 |
| Indoor | LHi | RF | −43.61 | 5.98 | 2.79 | 1.05 |
| Dense | LHi | RC | −40.42 | 5.40 | 2.81 | 2.33 |
| | LHi | REl | −38.85 | 5.34 | 2.48 | 2.53 |
| | LHi | RE | −40.75 | 5.74 | 2.58 | 2.07 |
| | LHi | RK | −39.13 | 4.68 | 2.46 | 2.97 |
| | LHi | Rhi | −40.01 | 5.22 | 2.78 | 3.31 |
| | LHi | RWr | −41.42 | 6.06 | 2.36 | 0.93 |

**Table 5.4** CM parameters: tangential polarisation

| | | | Channel | Gain | Shadowing | Fading |
|---|---|---|---|---|---|---|
| | Position 1 | Position 2 | $\mu_0$ (dB) | $\sigma_0$ (dB) | $\sigma_s$ (dB) | $K$ |
| Anechoic | LHi | RTi | −38.4 | 1.17 | 1.01 | 29.59 |
| | LHi | RWr | −53.09 | 2.89 | 3.98 | 5.83 |
| | LHi | LWr | −40.74 | 4.32 | 3.45 | 6.72 |
| | LHi | LE | −48.3 | 2.69 | 2.79 | 10.33 |
| | FC | RTi | −38.65 | 1.15 | 1.4 | 69.75 |
| | FC | RWr | −49.47 | 1.2 | 2.57 | 21.97 |
| | FC | LWr | −42.97 | 3.19 | 1.97 | 54.67 |
| | FC | LE | −46.82 | 4.57 | 1.5 | 17.34 |
| | RE | RTi | −57.57 | 1.84 | 3.17 | 1.44 |
| | RE | RWr | −53.31 | 3.19 | 2.89 | 7.40 |
| | RE | LWr | −57.57 | 0.91 | 1.72 | 0.00 |
| | RE | LE | −37.01 | 2 | 0.67 | 50.00 |
| Indoor | LHi | RTi | −60.77 | 4.89 | 3.05 | 4.79 |
| | LHi | RWr | −61.69 | 6.9 | 3.76 | 5.56 |
| | LHi | LWr | −49.62 | 2.95 | 7.22 | 8.68 |
| | LHi | LE | −64.26 | 3.3 | 2.38 | 3.58 |
| | FC | RTi | −62.72 | 2.41 | 1.82 | 3.00 |
| | FC | RWr | −60.15 | 5.79 | 2.99 | 3.39 |
| | FC | LWr | −58.35 | 1.5 | 4.21 | 5.56 |
| | FC | LE | −60.48 | 3.5 | 1.96 | 5.56 |
| | RE | RTi | −67.01 | 2.77 | 2.23 | 1.70 |
| | RE | RWr | −59.18 | 2.27 | 2.58 | 3.39 |
| | RE | LWr | −65.67 | 4.63 | 2.37 | 2.43 |
| | RE | LE | −54.67 | 4.73 | 2.15 | 5.95 |

and the angle a representing the body orientation with respect to the outer device (i.e., the off-body one).

*P*(*d,* $\alpha$), in dB, can be expressed according to:

$$P(d, \alpha) = G(d, \alpha) + F(d); \tag{5.6}$$

where *G*(*d*, $\alpha$) is the *mean channel gain* and *F*(*d*) represents the *fast fading* component, a random variable accounting for the multi-path contributions (MPCs) originating from the environment or from the body itself while moving. *G*(*d*, $\alpha$) can be described as:

$$G(d, \alpha) = G_0\,(d_0, \alpha) - 10 \cdot n(\alpha) \cdot \log_{10}\,(d/d_0); \tag{5.7}$$

where $G_0(d_0, \alpha)$ represents the mean channel gain evaluated at the reference distance $d_0$ = 1 *m* and $n(\alpha)$ is defined as the PL exponent.

**Table 5.5** Model parameters for mean channel gain: off-body scenario

| | LoS ($\alpha = 0^\circ$) | |
|---|---|---|
| | $n(0)$ | $G_0(d_0, 0)_{\|dBm}$ |
| Ext./Head | [1/1.6] | [–45.7/–50.2] |
| Ext./Upper Body | [1.7/2] | [–45.4/–51.7] |
| Ext./Lower Body | [0.4/1.6] | [–45/–47.8] |

Table 5.5 lists the numerical values derived for the mean channel gain, $G_0(d_0, \alpha)$, and the PL exponent, $n(\alpha)$. Results for the LoS case (i.e., a = 0°) are reported, referring to the scenarios where the subject was aligned to the external device. In order to characterise the *External Device/Head* communications, LoS values in Table 5.5 represents the case where nodes are placed on right ear while a generic subject is facing the outer device (Figure 5.18). Those values can be extended to other head parts, properly adapting $\alpha$ according to the subject head and trunk orientation.

When rotating, a channel gain correction factor can be applied according to the off-body ANT considered. Results in Table 5.6 are given normalised to the LoS case, representing in that way an additional attenuation to be added to the $G(d, 0^\circ)$ values reported in Table 5.5. Given the disparity of results here the results are given by distinguishing between the ANT polarisation on the body and the kind of ANT off-body. Generally when considering omnidirectional off-body ANT this is limited to the azimuth plane, and the main polarisation is

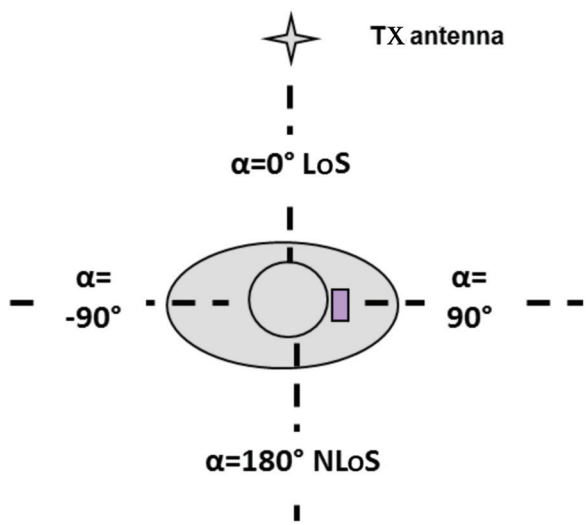


**Figure 5.18** LoS and NLoS conditions and body orientation $\alpha$.

**Table 5.6** Channel gain correction factors for intermediate off-body orientation: Body Shadowing effect

| Off-body ANT | Omni | | | Omni | | | Directive | | |
|---|---|---|---|---|---|---|---|---|---|
| On-body ANT | Tangential Pol. | | | Normal Pol. | | | Tangential Pol. | | |
| | 90° | 180° (NLoS) | −90° | 90° | 180° (NLoS) | −90° | 90° | 180° (NLoS) | −90° |
| Ext./Head | −5.4 | −3 | 6.6 | −5.2 | −2 | −8.4 | −12.2 | −5.7 | 9.9 |
| Ext./Upper Body | −7.7 | −20 | −14 | 6.4 | −12.8 | | −14.4 | −22 | −14.1 |
| Ext./Lower Body | – | – | – | – | – | – | 14.2 | −0.4 | −6.4 |

vertical with respect to the ground. On the other hand off-body directive ANT, also vertically polarised, is generally oriented towards the body, and typical gain is around 7 dBi.

As expressed by the general formula, besides the channel gain correction factor, the path LoSs expoinen is aLoS affected by the body rotation. The the PL exponent values in NLoS, i.e., $\boldsymbol{n}(\mathbf{180}^\circ)$, are generally vey low, between 0.25 and 0.6. Some specificic cases can be found with pathlosses closeto 1.5, for particular situations when the body orientation do not obstruct the LoS path, as for instance when the ANT is placed on a ear.

The statistic of the *fast fading* envelope is modelled by a Rice distribution, which is defined by the $K$ factor, the noncentrality and scale parameters, $\nu$ and $\alpha$, as reported in Table 5.7.

**Table 5.7** Fading characterisation for off-body CM

| | $\nu$ LoS | $\sigma$ LoS | $K$ LoS |
|---|---|---|---|
| Ext./Head | [0.8/0.9] | 0.3 | [3.6/4.5] |
| | $\nu$ NLoS | $\sigma$ NLoS | $K$ NLoS |
| | [1/1.1] | [0.6/0.7] | [1/1.7] |
| Ext./Upper | $\nu$ LoS | $\sigma$ LoS | $K$ LoS |
| | [0.9/1] | [0.5/0.6] | [1.1/2] |
| | $\nu$ NLoS | $\sigma$ NLoS | $K$ NLoS |
| | 0.001 | 0.9 | 0 |
| Ext./Lower | $\nu$ LoS | $\sigma$ LoS | $K$ LoS |
| | 1 | 0.3 | 5.6 |
| | $\nu$ NLoS | $\sigma$ NLoS | $K$ NLoS |
| | [0.9/1] | [0.5/0.7] | [0.8/2] |

The results here reported on fading statistics refer only to those scenarios were omnidirectional ANTs are used as off-body node. When using the directive ANTs, the LoS path could be enhanced, giving a higher $K$ factor (up to 35 in some scenarios). These results are not reported here, since they are strongly dependent on the angular selectivity properties of the off-body ANT, and cannot be generalised for a model, based on the measurements available.